ETH zürich

ETH Library

Selective Methane Oxybromination over Nanostructured Ceria Catalysts

Journal Article

Author(s):
Paunović, Vladimir; Zichittella, Guido; Mitchell, Sharon; Hauert, Roland; Pérez-Ramírez, Javier

Publication date:
2018-01-05

Permanent link:
https://doi.org/https://doi.org/10.3929/ethz-b-000231845

Rights / license:
In Copyright - Non-Commercial Use Permitted

Originally published in:
ACS Catalysis 8(1), https://doi.org/10.1021/acscatal.7b03074

Funding acknowledgement:
- Design of oxyhalogenation catalysts for hydrocarbon functionalization ()

This page was generated automatically upon download from the ETH Zurich Research Collection.
For more information, please consult the Terms of use.

Selective Methane Oxybromination over Nanostructured Ceria Catalysts

Vladimir Paunović,[†] *Guido Zichittella,*[†] *Sharon Mitchell,*[†] *Roland Hauert,*[§] *and Javier Pérez-Ramírez*[*,†]

[†] Institute for Chemical and Bioengineering, Department of Chemistry and Applied Biosciences, ETH Zurich, Vladimir-Prelog-Weg 1, CH-8093 Zurich, Switzerland

[§] EMPA, Swiss Federal Laboratories for Materials Science and Technology, Überlandstrasse 129, CH-8600 Dübendorf, Switzerland

ABSTRACT

This article studies the impact of the carrier type (MgO, SiO_2, SiC, Al_2O_3, ZrO_2) and synthesis method (dry impregnation, coprecipitation, hydrothermal synthesis, mechanochemical synthesis) on the structure, redox properties, and performance of supported CeO_2 catalysts for methane oxybromination. Major distinctions are evidenced in the product distribution with respect to bulk CeO_2, and the selectivity to methyl bromide (CH_3Br) varies in the following order: CeO_2/MgO (61-81%) > CeO_2/SiC (56-73%) ~ CeO_2/SiO_2 (52-71%) > bulk CeO_2 (40%) ~ CeO_2/ZrO_2 > CeO_2/Al_2O_3 (28-35%) at 6-40% methane conversion. The selectivity is primarily governed by the catalyst propensity to combust CH_3Br and byproduct dibromomethane (CH_2Br_2), which is strongly affected by the choice of the carrier. Specifically, the formation of carbon oxides is substantially suppressed over CeO_2 nanoparticles stabilized on basic MgO (CO_x selectivity <10%) with respect to bulk CeO_2 (CO_x selectivity ≥50%), whereas it is promoted by near atomic dispersions of CeO_2 on acidic ZrO_2 and Al_2O_3 carriers. Changes in the size and shape of CeO_2 nanoparticles on MgO had little impact on the selectivity, as they exhibit similar oxidation properties after exposure to the reaction environment. The synthesis-structure-performance relationships developed demonstrate the great potential of supporting CeO_2 to enhance the oxybromination performance.

KEYWORDS: natural gas upgrading, methane oxybromination, cerium oxide, support effects, magnesium oxide

1. INTRODUCTION

An amount of natural gas equivalent to about 18% of the US annual needs and worth *ca.* 13 billion USD is lost every year by flaring at far-flung fields (comprising >30% of known reserves) due to a lack of technologies enabling its economical on-site processing or transport to the centralized megaplants.[1-7] Among various routes that circumvent energy and capital intensive syngas generation,[8-14] the bromine-mediated upgrading of methane emerged as an attractive technology to valorize this stranded natural gas,[4,7,15-19] which has been demonstrated at plant scale.[20] It is based on the selective bromination of methane to methyl bromide (CH_3Br), the latter serving as a platform for the production of alcohols, ethers, gasolines, and aromatics *via* catalytic pathways similar to those of methanol. The feasibility of this technology relies on the efficient recovery of hydrogen bromide (HBr), which is formed in stoichiometric quantities in the bromination and subsequent CH_3Br upgrading steps.[4,7,19,21-24] Compared to the reaction of methane with molecular bromine, methane oxybromination (MOB) enables process intensification by using HBr and oxygen to convert methane into CH_3Br.[5,12,22-24] Dibromomethane (CH_2Br_2) is the only polybrominated byproduct in this reaction, which can be transformed to CH_3Br *via* reproportionation or hydrodebromination.[16,17,25] Still, the presence of oxygen in the reaction medium promotes combustion reactions, which is the main challenge for the implementation of MOB.[7,22]

Several catalysts, including bulk $(VO)_2P_2O_7$, $FePO_4$, and EuOBr phases, have demonstrated promising selectivity to CH_3Br in MOB and relatively low selectivity to CO_x ($S(CH_3Br) = 81\text{-}64\%$, $S(CO_x) \leq 15\ \%$ at methane conversions of $X(CH_4) = 14\text{-}30\%$).[22-24] In contrast, although CeO_2 would be an attractive candidate in view of its abundance and stability,[26-29] tests over the bulk phase evidenced significant combustion under equivalent conditions ($S(CO_x)$ = 30-45% at $X(CH_4)$ = 15-30%).[22-24]. Interestingly, similar to some other processes catalyzed by CeO_2,[30-34] the performance of this material in MOB was shown to be structure sensitive.[19] Substantially enhanced selectivity to CH_3Br was achieved by tailoring the nanocrystal morphology (up to $S(CH_3Br)$ = 75% at $X(CH_4)$ = 18% over nanocubes), which was further improved by the addition of NiO_x ($S(CH_3Br)$ = 82% at $X(CH_4)$ = 22%). Nonetheless, the formation of CO_x over nanocrystaline CeO_2 remained significant ($S(CO_x) \geq$17%).

In view of growing evidence that the formation of the C-Br bond in MOB results from the gas-phase reaction of methane with molecular bromine generated over the catalyst,[22,23] selectivity losses can be primarily associated with the surface catalyzed combustion of methane, CH_3Br, and CH_2Br_2. This can be approached by controlling *i*) the reaction conditions or *ii*) the catalyst properties, which are interlinked. Indeed, the evolution of CO_x over CeO_2 could be curbed by operating under a huge excess of HBr ($S(CO_x)$ = 2% at $X(CH_4)$ = 20%), which was ascribed to the controlled surface reduction due to bromination of the outward catalyst structure under reaction conditions.[23] Another well-known strategy that allows tailoring of the geometric and electronic properties of CeO_2 catalysts comprises the dispersion over a suitable carrier.[27,35-42] However, despite constituting a pivotal step towards catalyst scale-up, the impact of supporting of CeO_2 on the MOB performance has not been studied previously.

Herein, CeO_2 catalysts supported over commonly applied carriers: SiO_2, SiC, Al_2O_3, ZrO_2, and MgO using different synthesis methods and relatively low active phase loading ($\leq$2 wt.% CeO_2) are investigated in MOB. Their performance is correlated to the catalyst structure, its oxidizing potential, and propensity to brominate, as well as to the activity of the support in side combustion reactions. It is shown that supported CeO_2 catalysts might display substantially enhanced selectivity to CH_3Br and CH_2Br_2 and highly suppressed CO_x production.

2. EXPERIMENTAL

2.1. Catalyst preparation. Bulk CeO_2 (Sigma-Aldrich, nanopowder, 99.9%) was calcined at 973 K for 5 h in static air (heating rate 5 K min^{-1}) prior to the catalytic tests. If not stated otherwise, MgO (~20 nm, Strem Chemicals, ≥99%), SiO_2 (20-60 μm, Evonik, AEROPERL® 300/30, ≥99.0%), SiC (<100 nm, Sigma-Aldrich, ≥99%), ZrO_2 (≤60 μm, Alfa-Aesar, 99%), and γ-Al_2O_3 (5-100 μm, Sasol, PURALOX® SCFa 140, ≥98%) were calcined using the same protocol as that for CeO_2 and stored under vacuum (50 mbar) at 373 K prior to their use as supports in the catalyst preparation.

Dry impregnation was used as a standard method to prepare CeO_2 catalysts supported over various carriers. Herein, $Ce(NO_3)_3 \cdot 6H_2O$ (Aldrich, 99.9%) was dissolved in a volume of deionized water equal to the pore volume of the carrier in appropriate amounts to achieve 2 wt.% loading of CeO_2. The precursor solutions were added dropwise to the carrier and the resulting materials were periodically mixed at room temperature for 1 h, then dried under vacuum (50 mbar) at 373 K for 12 h, and finally calcined in static air at 973 K for 5 h (heating rate 5 K min^{-1}). These catalysts were referred to as CeO_2/*S*, where *S* denotes the carrier.

Using an analogous protocol, a set of MgO-supported catalysts were prepared with reduced CeO_2 loading (0.1 and 0.5 wt.%, referred to as CeO_2/MgO-0.1 and CeO_2/MgO-0.5, respectively). A second series of catalysts with a CeO_2 loading of 0.5 wt.% were synthesized varying the temperature of the final calcination step (973, 1173, or 1373 K, denoted as CeO_2/MgO-0.5-973, CeO_2/MgO-0.5-1173, CeO_2/MgO-0.5-1373, respectively). In this case, the MgO carrier was calcined at 1373 K prior to use.

MgO-supported CeO_2 (2 wt.%) catalysts were also prepared by mechanochemical synthesis, coprecipiation, and hydrothermal synthesis. Mechanochemical synthesis was performed by introducing $Ce(NO_3)_3·6H_2O$ on the MgO carrier by impregnation. The resulting materials was transferred to a stainless steel jar (50 cm^3), filled with 12 stainless steel balls (d_{ball} = 10 mm, W_{ball} = 7.8 g) and ground in a planetary ball mill (Retch PM 200) for 4 h (500 rpm). Coprecipitation was conducted starting from a solution containing 0.006 M $Ce(NO_3)_3·6H_2O$ and 1.2 M $Mg(NO_3)_2·6H_2O$, which was prepared by dissolving the metal salts in deionized water (200 cm^3). Hydrogen peroxide (53 cm^3, Aldrich, 35 wt.%) was then added and the solution was stirred (500 rpm) for 1 h. Subsequently, aqueous ammonium hydroxide (Merck, 25 wt. %) was added dropwise until reaching a pH of 10, and the resulting slurry was aged for 2 h under stirring. The solids were recovered by filtration and washed with deionized water. For hydrothermal synthesis, MgO was suspended in a 6 M solution of NaOH (Fisher Chemicals, 99%) in deionized water (40 cm^3). A 0.4 M solution of $Ce(NO_3)_3·6H_2O$ in deionized water (1.8 cm^3) was mixed with this slurry, stirred (500 rpm) for 2 h, then transferred into a Teflon-lined autoclave (50 cm^3), and hydrothermally treated at 453 K for 24 h. The solid was collected by filtration and washed with deionized water. The materials recovered after mechanochemical synthesis, coprecipitation, and hydrothermal synthesis were dried and calcined as described above for dry impregnation. The resulting catalysts were denoted as CeO_2/MgO-m, CeO_2/MgO-c, and CeO_2/MgO-h, respectively.

2.2. Catalyst characterization. Powder X-ray diffraction (XRD) was measured using a PANalytical X'Pert PRO-MPD diffractometer with Bragg-Brentano geometry by applying Cu-Kα radiation (λ = 1.54060 Å). The data were recorded in the 10-70° 2θ range with an angular step size of 0.017° and a counting time of 2.04 s per step. The average size of CeO_2 crystallites was estimated from the broadening of the {111} reflection of CeO_2 by using Scherrer equation with dimensionless shape factor, K = 0.9. N_2 sorption at 77 K was performed using a

Micromeritics TriStar analyzer. Samples were evacuated to 50 mbar at 573 K for 12 h prior to the measurement. The Brunauer-Emmett-Teller (BET) method was applied to calculate the specific surface area, S_{BET}. The pore volume of the catalyst carriers, V_{pore}, was determined from the amount of N_2 adsorbed at a relative pressure of $p/p_0 = 0.98$. The total cerium content in the supported catalysts was quantified by inductively coupled plasma optical emission spectroscopy (ICP-OES) using a Horiba Ultima 2 instrument equipped with photomultiplier tube detection. High-resolution transmission electron microscopy (HRTEM), high-angle annular dark field scanning transmission electron microscopy (HAADF-STEM), and elemental mapping with energy-dispersive X-ray spectroscopy (EDXS) were conducted on a FEI Talos microscope operated at 200 kV. All samples were dispersed as dry powders onto lacey carbon coated nickel grids. The average size of CeO_2 nanoparticles was calculated by examining over 50 nanoparticles. Fast Fourier transforms of selected areas of HRTEM images were calculated using ImageJ software. Raman spectroscopy was performed on a WITec CRM200 confocal Raman system using a 532 nm laser with 20 mW power, a 100× objective lens with numerical aperture NA = 0.9 (Nikon Plan) and a fiber-coupled grating spectrometer (2400 lines per mm), giving a spectral sampling resolution of 0.7 cm^{-1}. X-ray photoelectron spectroscopy (XPS) measurements were performed on a Physical Electronics Quantum 2000 X-ray photoelectron spectrometer using monochromatic Al-Kα radiation, generated from an electron beam operated at 15 kV, and equipped with a hemispherical capacitor electron-energy analyzer. The solids were analyzed at an electron take-off angle of 45° and a pass energy of 46.95 eV. In order to suppress sample charging during analysis an electron and an ion neutralizer were operated simultaneously. Remaining charging effects were corrected by referencing all spectra to adventitious carbon (C 1*s* at 284.5 eV). The elemental concentrations were quantified based on the measured photoelectron peak areas (Br 3*d*, Ce 3*d*) after Shirley background subtraction using PHI-MultiPak software and the built-in relative sensitivity factors, which are corrected for the system transmission function. The fractions of different oxidation states of cerium were estimated by deconvolution of the Ce 3*d* peak.

2.3. Catalyst testing. Methane oxybromination, and CO, CH_3Br, CH_2Br_2, and HBr oxidation were performed at ambient pressure in a continuous-flow fixed-bed reactor setup (**Figure S1**), which has been described previously.[24] Gases: CH_4 (PanGas, purity 5.0), HBr (Air Liquide, purity 2.8, anhydrous), O_2 (PanGas, purity 5.0), CH_3Br (PanGas, 5 mol% in He 5.0), CO (Messer, 5 mol% in He 5.0), Ar (PanGas, purity 5.0; internal standard), and He (PanGas, purity 5.0; carrier gas), were supplied by a set of digital mass-flow controllers (Bronkhorst) to the mixing unit equipped with pressure indicator, and CH_2Br_2 (ABCR, 99%) was fed using a syringe pump (Nexus 6000, Chemyx) with a water-cooled glass syringe (Hamilton, 1 cm^3) connected to a vaporizer operated at 343 K. A quartz reactor (internal diameter, d_i = 8 mm) was loaded with the catalyst (catalyst weight, W_{cat} = 0.2-1 g, particle size, d_p = 0.4-0.6 mm), which was well-mixed with quartz particles (Thommen-Furler, d_p = 0.2-0.3 mm) to ensure a constant bed volume (V_{bed} = 2 cm^3), and placed in a homemade electrical oven. A K-type thermocouple fixed in a coaxial quartz thermowell with the tip positioned in the center of the catalyst bed was used to monitor the temperature during the reaction. Prior to testing, the catalyst bed was heated in a He flow to the desired temperature (T = 423-823 K) and allowed to stabilize for at least 30 min before the reaction mixture was fed. The catalyst weights, total flow rates (F_T), and feed mixtures applied in the tests are summarized in **Table 1**.

Carbon-containing compounds (CH_4, CH_3Br, CH_2Br_2, CO, and CO_2) and Ar were quantified on-line *via* a gas chromatograph equipped with a GS-Carbon PLOT column coupled to mass spectrometer (GC-MS, Agilent GC 6890, Agilent MSD 5973N). Quantification of Br_2 at the reactor outlet was performed by its absorption in an impinging bottle filled with 0.1 M KI solution ($Br_2 + 3I^- \rightarrow I_3^- + 2Br^-$) followed by iodometric titration (Mettler Toledo G20 Compact Titrator) of the formed triiodide ($I_3^- + 2S_2O_3^{2-} \rightarrow 3I^- + S_4O_6^{2-}$) with 0.01 M sodium thiosulfate solution (Aldrich, 99.99%).

The conversion of reactant *i*, $X(i)$, (*i*: CH_4, CH_3Br, CH_2Br_2, or CO) was calculated using Eq. 1,

$$X(i) = \frac{n(i)^{\text{inlet}} - n(i)^{\text{outlet}}}{n(i)^{\text{inlet}}} \cdot 100,\ \% \qquad \text{Eq. 1}$$

where $n(i)^{\text{inlet}}$ and $n(i)^{\text{outlet}}$ are the are the respective molar flows of the reactant *i* at the reactor inlet and outlet.

The conversion of HBr, X(HBr), was calculated according to Eq. 2,

$$X(\text{HBr}) = \frac{2 \cdot n(\text{Br}_2)^{\text{outlet}}}{n(\text{HBr})^{\text{inlet}}} \cdot 100,\ \% \qquad \text{Eq. 2}$$

where $n(\text{Br}_2)^{\text{outlet}}$ and $n(\text{HBr})^{\text{inlet}}$ denote the respective molar flows of bromine and HBr at reactor outlet and inlet.

The reaction rate, *r*, expressed with respect to the reactant *i* (*i*: CH_4, CH_3Br, CH_2Br_2, or CO) was calculated using Eq. 3,

$$r = \frac{n(i)^{\text{inlet}} - n(i)^{\text{outlet}}}{W_{\text{cat}}},\ \text{mol}(i)\ \text{s}^{-1}\ \text{g}_{\text{cat}}^{-1} \qquad \text{Eq. 3}$$

The selectivity to product *j*, $S(j)$, and the yield of product *j*, $Y(j)$, (*j*: CH_3Br, CH_2Br_2, CO, CO_2) were calculated using Eqs. 4 and 5, respectively,

$$S(j) = \frac{n(j)^{\text{outlet}}}{\sum^{\text{outlet}} n(j)^{\text{outlet}}} \cdot 100,\ \% \qquad \text{Eq. 4}$$

$$Y(j) = \frac{X(i) \cdot S(j)}{100}, \% \quad \text{Eq. 5}$$

The error of the carbon mass balance, ε_C, determined using Eq. 6,

$$\varepsilon_C = \frac{\sum^{\text{inlet}} n(i)^{\text{inlet}} - \left(n(CH_4)^{\text{outlet}} + \sum^{\text{outlet}} n(j)^{\text{outlet}} \right)}{\sum^{\text{inlet}} n(i)^{\text{inlet}}} \cdot 100, \% \quad \text{Eq. 6}$$

was less than 5% in all experiments.

The absence of external heat and mass transfer limitations were confirmed by calculating Carberry number and the criteria given by Mears,[43,44] respectively, while the internal mass transfer limitations can be discarded based on the experiments in which the particle size of the representative catalysts was varied (**Table S1**). The measurements of the bed temperature along its axial coordinate, showed the variation of $\leq$0.2 K.

After the tests, the reactor was quenched to room temperature in He flow and the catalyst was retrieved for characterization studies.

3. RESULTS AND DISCUSSION

3.1. Characterization of fresh catalysts. To study the effect of dispersing ceria on the performance in methane oxybromination, the first task was to assess the impact of the carrier. For this purpose, supported catalysts containing equivalent amounts of CeO_2 (2 wt.%) were prepared by dry impregnation applying five representative supports (leading to samples coded CeO_2/S, where S = MgO, SiO_2, SiC, Al_2O_3, or ZrO_2). Analysis by X-ray diffraction (XRD) pointed towards differences in the dispersion of CeO_2 depending on the carrier applied (**Figure 1**). In particular, while broad weak reflections, characteristic of the presence of cubic CeO_2 nanocrystals with an estimated average size of *ca.* 4-9 nm (**Table 2**) were visible in

CeO_2/MgO, CeO_2/SiO_2, and CeO_2/SiC, they were absent in the diffractograms of CeO_2/Al_2O_3 and CeO_2/ZrO_2. Consistently, examination by high angle annular dark field scanning transmission electron microscopy (HAADF-STEM) coupled with elemental mapping confirmed the presence of CeO_2 nanoparticles decorating the surface of the MgO, SiO_2, and SiC carriers (**Figure 2**), contrasting the near atomic dispersion of the active phase on Al_2O_3 or ZrO_2. Subtle differences could be noted in the average size and morphology of the supported CeO_2 nanoparticles (**Table 2**), appearing bigger on MgO (*ca*. 6 nm) and SiC (*ca*. 9 nm) compared to SiO_2 (*ca*. 4 nm), which is likely related to the high surface area of the latter, and presenting a higher aspect ratio on MgO with respect to the spherical-like particles observed on SiO_2 and SiC (**Figure 3**, **Figure S2**). High-resolution transmission electron microscopy (HRTEM) revealed that the CeO_2 nanoparticles dominantly expose the {111} facets with a *d*-spacing of 0.31 nm, in line with their higher thermodynamic stability.[19,33,34] In line with XRD and electron microscopy analysis, the Raman spectra of bulk CeO_2, CeO_2/MgO, CeO_2/SiO_2, and CeO_2/SiC (**Figure 4**) displayed a peak located at 461–464 cm^{-1}, which is ascribed to the F_{2g} mode of nanocrystalline fluorite structure of CeO_2.[37,38,40,45] Contrastingly, the spectra of CeO_2/ZrO_2, which shows only the bands ascribed to the monoclinic ZrO_2 support, and CeO_2/Al_2O_3, which shows no Raman active bands in the spectral region of interest, are indicative of high ceria dispersion over these carriers and point to the possible formation of $Ce_xZr_{1-x}O_2$ and $CeAlO_3$ (*vide infra*).[46,47] The latter compound is known to exhibit no active peaks in the investigated spectral range.[47] Bulk CeO_2 also exhibited a weak peak at 246 cm^{-1}, which is attributed to the second-order transverse acoustic mode (2TA).[45] In the case of CeO_2/SiO_2, a low-intensity peak at 604 cm^{-1} is ascribed to a defect induced mode of CeO_2.[37,45] This mode, which is normally Raman inactive, is correlated to the increased concentration of the oxygen vacancy defects and is often observed in silica supported ceria catalysts.[37] The feature at 144 cm^{-1} in the spectrum of CeO_2/MgO is likely originating from MgO support, while the peak located at 512 cm^{-1} in the spectrum of CeO_2/SiC is related to Si-Si bonds in SiC.[48]

To confirm the effect of dispersing the active phase on the electronic properties of ceria, the supported catalysts were analyzed by X-ray photoelectron spectroscopy (XPS, **Figure S3**). Both Ce^{3+} and Ce^{4+} species could be identified based on the satellite peaks observed around the 3*d* peaks of ceria.[49] Analysis of the relative composition of these species indicated that CeO_2/MgO and CeO_2/SiC contained predominantly Ce^{4+} (>93% Ce^{4+}, <7% Ce^{3+}) consistent with the distribution expected for CeO_2 (**Figure 5a**).[49] Comparatively, appreciable amounts of Ce^{3+} were observed for CeO_2/SiO_2 (*ca*. 33% Ce^{4+}), and particularly CeO_2/ZrO_2 (*ca*. 45% Ce^{4+}) and CeO_2/Al_2O_3 (*ca*. 52% Ce^{4+}). Considering the high ceria dispersion observed in the latter materials, these results also suggest that a significant portion of cerium is likely present in the form of $CeAlO_3$ or $Ce_xZr_{1-x}O_2$ solid solutions, respectively, due to the reaction with support,[14,37,41,47] while the formation of CeO_2-silica compounds might also be possible in the case of CeO_2/SiO_2.[50] In other words, the interaction of ceria with SiO_2, and particularly Al_2O_3 and ZrO_2 support appears to be stronger compared to MgO and SiC. It is noteworthy that the CeO_2/SiC catalyst exhibited a strong O 1*s* signal (**Figure S3**), with a surface O:Si ratio of *ca.* 1.9, which is consistent with HRTEM observations (**Figure S2**) suggesting the formation of a silica-like structure at the surface of SiC.

Different molecules such as H_2, CO, O_2, or methane can be used to probe the reactivity of oxygen species in oxide-based catalysts by temperature-programmed reactions, which can be conducted in the form of transient (non-stationary) or steady state tests.[27,33] The redox properties of the bulk and supported CeO_2 catalysts were here assessed using CO oxidation. This reaction is expected to proceed *via* a Mars-van Krevelen mechanism, in which CO reacts with surface bound oxygens of ceria, and thus is sensitive to the structure and surface-related oxidation potential of the catalyst.[27,33] The rates of CO oxidation at 753 K (**Figure 5b**), which were extracted from the representative light-off curves (**Figure S4**), decrease as follows: bulk CeO_2 >> CeO_2/ZrO_2 > CeO_2/MgO > CeO_2/SiC ~ CeO_2/Al_2O_3 > CeO_2/SiO_2, indicating that the oxidizing potential of the supported catalysts is significantly (*ca*. 2-40 times) reduced compared to bulk CeO_2. This could benefit the performance in MOB, since the strongly oxidizing character of bulk CeO_2 promotes combustion, resulting in a selectivity loss. [22-24] The activity of the catalysts in CO oxidation were also compared based on the apparent activation energy (**Figure 5b**), which was calculated from the linear region of Arrhenius plots that corresponds to 5-40% of CO conversion (**Figure S4**). The values of this parameter were in the range of 40-100 kJ mol^{-1} and increased in the following order: CeO_2/SiC < CeO_2 ~ CeO_2/ZrO_2 ~ CeO_2/MgO < CeO_2/Al_2O_3 < CeO_2/SiO_2, corroborating the previous observation that CO oxidation is particularly hampered over the fresh CeO_2/Al_2O_3 and CeO_2/SiO_2 catalysts.

3.2. Evaluation of catalysts in methane oxybromination. The bulk and supported CeO_2 catalysts were evaluated in MOB at three different temperatures (753, 773, and 793 K), using a stoichiometric ratio of reactants (CH_4:HBr:O_2 = 2:2:1) in the feed (**Figure 6**). The conversion of methane was in the range of 6-40%, which is comparable to those previously reported.[19,22-24] MOB activity decreased in the following order: CeO_2/SiO_2 > CeO_2/SiC > CeO_2/ZrO_2 > bulk CeO_2 > CeO_2/MgO > CeO_2/Al_2O_3, wherein the most active CeO_2/SiO_2 catalyst displayed a 2-2.8 times higher activity compared to the least active CeO_2/Al_2O_3. Nevertheless, the rates over the other supported catalysts, *i.e.*, CeO_2/SiC,

CeO_2/ZrO_2, and CeO_2/MgO showed much smaller differences (5-30%) and were comparable to those over bulk CeO_2. Consistently, the apparent activation energies (**Figure S5**), which ranged from 80-156 kJ mol^{-1}, increased in a similar order: CeO_2/SiO_2 (80 kJ mol^{-1}) ~ CeO_2/ZrO_2 < CeO_2/SiC (100 kJ mol^{-1}) < CeO_2 (110 kJ mol^{-1}) < CeO_2/MgO (120 kJ mol^{-1}) < CeO_2/Al_2O_3 (156 kJ mol^{-1}).

As exemplified for several catalysts (**Figure 6**), the selectivity-conversion curves followed the same trend when the conversion was controlled by adjusting the reaction temperature or the space velocity. Supported CeO_2 systems displayed remarkable differences in product distribution compared to bulk CeO_2. Significantly enhanced selectivity to CH_3Br was observed over CeO_2/MgO (61-81%), CeO_2/SiC (56-73%), and CeO_2/SiO_2 (52-71%) compared to CeO_2/ZrO_2, which was similar to bulk CeO_2 (*ca*. 40%), while the lowest selectivity to this product was obtained over CeO_2/Al_2O_3 (28-35%). This could be linked to the selectivity to CO_x, which increased in the opposite order: CeO_2/MgO (6-11%) < CeO_2/SiC (9-21%) < CeO_2/SiO_2 (17-34%) < CeO_2/ZrO_2 (*ca*. 50%) ~ bulk CeO_2 < CeO_2/Al_2O_3 (30-65%). The most prominent byproduct over the best-performing CeO_2/MgO catalyst was CH_2Br_2, which although less valued than CH_3Br, could be further valorized in bromine-meditated natural gas upgrading *via* reproportionation or hydrodebromination.[9,10,25] The yield of CH_3Br (≤18.7%), as well as the combined yield of CH_3Br and CH_2Br_2 (≤25.9%) are among the highest reported in the literature.[19,22-24] To confirm the catalyst stability, the activity of CeO_2/MgO was evaluated under more demanding conditions of moderate conversion and decreased oxygen content in the feed (**Figure 7**). Remarkably, the performance of this catalyst was stable over 80 h on stream.

3.3. Characterization of the used catalysts. The structure, porosity, and electronic properties of the oxyhalogenation catalysts can be altered under reaction conditions. To determine the impact of the reaction environment on these properties, the bulk and supported CeO_2 catalysts were characterized after equilibration in MOB at 773 K over 5 h. The specific surface areas and pore volumes of the supported catalysts were essentially unaltered after this test, confirming the stability of the respective carriers, while bulk CeO_2 experienced *ca.* 20% decrease (**Table 2**). The XRD patterns of the equilibrated catalysts resembled those of the respective fresh materials (**Figure 1**), demonstrating the absence of structural alterations, such as the formation of bromide phases, which is consistent with the previously reported stability of CeO_2 in this reaction.[19,23]. The HAADF-STEM micrographs of CeO_2/MgO catalyst evidenced an increased prevalence of rod-like CeO_2 nanoparticles (length: 5-12 nm, width: 2-3 nm) along the edges of MgO particles, although the average particle size assuming a spherical geometry was unaltered (6 nm) (**Figure 2f**, **Table 2**). Comparatively, the size of CeO_2 nanoparticles in the equilibrated CeO_2/SiO_2 (**Figure 2g**) and CeO_2/SiC (**Figure 2h**) matched those of the respective fresh catalysts (**Table 2**). HRTEM analysis of CeO_2/MgO (**Figure 3b**) and CeO_2/SiO_2 (**Figure 3d**) demonstrated that the {111} type facets remain predominant, although {200} facets (with a *d*-spacing of 0.27 nm) were also observable (**Figure S2**).[19,33,34] HAADF-STEM micrographs and elemental maps indicated that the dispersion of ceria in equilibrated CeO_2/ZrO_2 (**Figure 2i**) and CeO_2/Al_2O_3 (**Figure 2j**) remained close to atomic. Consistently, the Raman spectra of the equilibrated catalysts (**Figure 4**) displayed no significant differences compared to the fresh samples. The only exception was CeO_2/SiC, wherein the peak at 512 cm^{-1} ascribed to Si-Si bond in SiC support vanished upon its exposure to the oxybromination, likely due to carrier oxidation into SiO_2. Elemental maps also suggest that a higher amount of bromine was taken up by the

CeO_2/MgO and CeO_2/Al_2O_3 catalysts compared to the other materials (**Figure 2**). This was substantiated by the increased Br:Ce ratio evidenced by XPS in the surface of the equilibrated catalysts, which followed the trend: $CeO_2/MgO > CeO_2/Al_2O_3 > CeO_2/ZrO_2 > CeO_2/SiO_2 > CeO_2/SiC$ (**Figure 5a**). Analysis of the Ce 3*d* core level spectra of equilibrated CeO_2/MgO, CeO_2/SiC, CeO_2/ZrO_2, and CeO_2/SiC revealed a slightly lower fraction of Ce^{4+} compared to the fresh catalysts, suggesting a partial reduction of ceria (**Figure 5a**, **Figure S3**). In contrast, an increased fraction of Ce^{4+} was observed for CeO_2/SiO_2. Since the bromination of CeO_2 is expected to induce reduction, *i.e.*, a decrease in the fraction of Ce^{4+} state,[24] the increased bromine content of CeO_2/MgO is likely related to the bromination of the carrier, which could be expected due to its strong basic character. This was supported by the good correlation between the bromine and magnesium signals in the elemental maps (**Figure 2f**). Still, the surface Br:Mg ratio of *ca*. 0.03 determined from XPS was well below that expected for $MgBr_2$, indicating that the bromination of MgO is partial and/or constrained to the outer most layers of the carrier. Another interesting feature was the change of the redox properties of the catalysts after use in MOB, as evidenced by the change in CO oxidation rates compared to the fresh catalysts (**Figure 5b**, **Figure S4**). The equilibration of CeO_2/Al_2O_3, CeO_2/ZrO_2, CeO_2/SiC, and CeO_2/SiO_2 led to an increase in their CO oxidation activity, which was particularly pronounced for the latter two materials. It is hypothesized that MOB induced decomposition of ceria-silica compounds that could be present in the fresh CeO_2/SiC and CeO_2/SiO_2 catalysts, yielding smaller ceria crystallites, which are more active in oxidation.[36,50] This may also explain the noticeable increase in the Ce^{4+} fraction in the equilibrated CeO_2/SiO_2 catalyst (**Figure 5a**). In contrast, CeO_2/MgO showed similar behavior to bulk CeO_2, both catalysts exhibiting a lower rate and higher apparent activation energy with respect to the fresh materials. The decreased oxidizing potential of CeO_2/MgO could be related to the growth of the rod-like CeO_2 nanoparticles, which exhibited a slightly increased size compared to those present in the fresh catalyst. Nevertheless, these structural changes appear to be of a much lower magnitude compared to the more than 50% decrease in the CO oxidation rate. It seems more plausible that the reduction of the oxidizing propensity of the equilibrated CeO_2/MgO is related to its bromination, which as discussed above primarily occurs on the support. It might also be possible that CeO_2 nanoparticles are doped or decorated with MgO, which after being brominated reduces their ability to oxidize CO as well as bromomethanes.

3.4. Optimization of MgO-supported CeO_2 catalysts. Given the remarkable performance of CeO_2/MgO catalyst in MOB, this system was chosen to evaluate the role of morphology of supported CeO_2 phase on its activity and product distribution. In this regard, the loading of CeO_2 and the synthesis method were adjusted to tailor the geometry of CeO_2 nanoparticles, and hence to determine their impact on the MOB performance. As the CeO_2/MgO catalyst exhibited an activity comparable to that of bulk CeO_2 (**Figure 6**), the effect of reducing the CeO_2 loading to 0.5 and 0.1 wt.% (*i.e.*, CeO_2/MgO-0.5 and CeO_2-MgO-0.1) and the contribution of the bare MgO carrier were evaluated in MOB (**Figure 8**, left). Decreasing the content of the active phase led to the expected reduction in the rate of MOB. Nevertheless, the activity of CeO_2/MgO-0.5 was only *ca*. 10% lower compared to that of CeO_2/MgO, while the product distribution was essentially unaffected. Inspection of the equilibrated CeO_2/MgO-0.5 catalyst revealed a similar size (*ca*. 6 nm), shape, and faceting of CeO_2 nanoparticles as observed in CeO_2/MgO (**Figure 9a**, **Figure S6**, **Table 2**), although no rod-like nanostructures could be observed. In the case of CeO_2/MgO-0.1, the particles of CeO_2 could not be clearly distinguished (**Figure S7**). Its activity was significantly lower and selectivity to CO_x enhanced, and was in this regard more similar to the bare MgO. Although the latter carrier exhibited a relatively high selectivity to CH_3Br, it led to a more pronounced CO_x production compared to CeO_2/MgO. Besides, activity of MgO and the yield of bromomethanes over this material are ca. 4-5 times lower compared to CeO_2/MgO, which preserves the high selectivity to bromomethanes and low selectivity to CO_x at significantly higher conversions. This result indicates that CeO_2 is primarily responsible for the activity of the supported catalysts.

To confirm the impact of the particle size on the performance of CeO_2 nanoparticles supported on MgO, catalysts with a CeO_2 loading of 0.5 wt.% were calcined at three different temperatures (973, 1173, and 1373 K). The resulting samples (*i.e.*, CeO_2/MgO-0.5-973, CeO_2/MgO-0.5-1173, and CeO_2/MgO-0.5-1373) displayed comparable surface areas (**Table 2**), while the average size of CeO_2 nanoparticles increased from *ca*. 6 to 15 nm with increasing calcination temperature (**Figure S7**, **Table 2**). The rate of MOB decreased with increasing the particle size (**Figure 8**, middle). Nevertheless, the selectivity-conversion patterns for these catalysts followed an almost identical trend as the one observed for CeO_2/MgO catalyst, suggesting the absence of a noticeable particle size effect on the product distribution in MOB over this catalytic system.

Besides, to further probe the impact of the particle geometry and their interaction with the support on MOB, supported CeO_2 catalysts (2 wt.%) were prepared by coprecipitation, mechanochemical, and hydrothermal synthesis (*i.e.*, CeO_2/MgO-c, CeO_2/MgO-m, and CeO_2/MgO-h, respectively). The average size of the CeO_2 nanoparticles in these materials was similar to or slightly larger than that of CeO_2/MgO (**Figure 9**, **Table 2**). In the equilibrated CeO_2/MgO-c catalyst {111} fringes were prevalent, although the particles also exposed {200} facets, while CeO_2/MgO-h displayed CeO_2 nanocubes dominated by {200} facets. CeO_2/MgO-c exhibited the highest reaction rate (**Figure 8**, right), exceeding that of the reference CeO_2/MgO catalysts (**Figure 8**, left), at almost similar selectivity to bromomethanes. The activity and selectivity profiles of CeO_2/MgO-h and CeO_2/MgO-m catalysts were analogous to those of CeO_2/MgO. Overall, these results indicate that CeO_2 nanostructure has a minor effect on the product distribution over MgO supported CeO_2 catalysts. This contradicts previous findings of He *et al*. who reported the structure sensitive performance of CeO_2 in MOB based on the study of well-defined nanocrystals of CeO_2, wherein the nanocubes, *i.e.*, {200} facets were found the most active and selective.[19] However, it has to be noted that the differences in product distribution and particularly the reaction rates between the different CeO_2 nanoparticles observed by these authors were not so strongly pronounced (*ca.* ±10%).

Consistently, the CO oxidation activity of the various MgO-supported CeO_2 catalysts was almost identical after their equilibration in MOB, and substantially lower compared to that of the fresh catalysts, for which significant differences in the redox properties could be observed (**Figure 10**, **Figure S8**). This result indicates that the different MgO supported catalysts possess a very similar oxidizing potential under MOB environment, likely caused by the catalyst bromination, which ultimately result in the very similar product distribution.

3.5. Rationalization of the product distribution. Our previous studies on MOB over bulk catalytic systems suggested that the formation of C-Br bonds might involve the gas-phase reaction of methane with bromine that is generated by the HBr oxidation on the catalysts (**Figure 11**).[22-24] Several kinetic fingerprints, such as *i*) the occurrence of MOB in the temperature window (≥753 K) which coincides with that of the non-catalyzed gas-phase bromination, *ii*) comparable MOB rates over bulk and supported CeO_2 catalyst in spite of their markedly different redox properties, *iii*) selectivity to CH_3Br and CH_2Br_2 over the best performing CeO_2/MgO catalyst which is similar to those in the gas-phase bromination, and *iv*) the absence of the sensitivity of the product distribution on the size and faceting of CeO_2 nanoparticles (**Figure 8**) give strong hints that this mechanism might also operate in the case of supported CeO_2 catalysts. To shed a light on the origin of MOB activity, the equilibrated bulk and supported CeO_2 catalysts were also evaluated in methane and HBr oxidation (**Figure 12a**, **Figure S9**), which were applied as the probe reactions to access the catalyst ability to activate these reactants. Herein, the rates of methane oxidation over bulk CeO_2 and CeO_2/ZrO_2 catalyst were *ca.* 2-3 times lower compared to those of MOB (**Figure S9**), implying that there could be a catalytic contribution in the latter reaction. This result also correlates with the strong oxidizing potential of the latter catalysts (**Figure 5b**). Nevertheless, a catalytic activation of methane over these materials is likely contributing to a pronounced CO_x evolution in MOB (**Figure 6**). Contrastingly, the rates of CH_4 oxidation over CeO_2/MgO, CeO_2/SiO_2, CeO_2/SiC, and CeO_2/Al_2O_3 were *ca.* 5-10 times lower compared to those in MOB (**Figure S9**), suggesting that methane activation over these catalysts is substantially impeded. In fact, this set of catalysts displayed a great selectivity enhancement in MOB, with the exception of CeO_2/Al_2O_3 (**Figure 6**). On the other hand, the rates of HBr oxidation were >8 times higher compared to those of MOB (**Figure 12a**, **Figure S9**), indicating the facile evolution of bromine, which may enter the gas-phase bromination reaction (**Figure 11**). The feasibility of the mechanism comprising heterogeneous HBr oxidation and gas-phase bromination of methane was also probed by studying the reaction kinetics over the most selective CeO_2/MgO catalyst in more detail (**Figure S11**). The apparent reaction order with respect to methane of *ca.* 1 (**Figure S11**) displayed by this catalyst was close to that observed in methane bromination (*ca.* 1).[51] The order with respect to HBr of *ca.* 0.2 (**Figure S11**), which might appear in contrast to the known inhibition effect of this reactant on the gas-phase bromination,[51] can be explained by the continuous oxidation of HBr into Br_2, to which the gas-phase bromination exhibits a positive reaction order (*ca*. 0.5).

In the above proposed mechanism the principal role of a catalyst is to oxidize HBr into molecular bromine and to suppress a loss of selectivity to bromomethanes by suppressing the combustion reactions (**Figure 11**). The propensity of CeO_2 catalysts supported over different carriers to evolve CO_x in MOB (**Figure 6**) generally agreed with the order of catalysts activity in CO oxidation after the equilibration (**Figure 5b**). In agreement with our previous findings on bulk systems,[21,22] this result indicates that the product distribution is primarily determined by the redox properties of the catalyst (**Figure 11**). The exception to this rule was the CeO_2/Al_2O_3 catalyst, which although exhibiting a slightly higher CO oxidation activity compared to the best performing CeO_2/MgO catalyst (**Figure 5b**), displayed the lowest selectivity to bromocarbons in oxybromination. A possible explanation for this exceptional behavior, might be the activity of the carrier in the undesired combustion reactions, comprising the oxidation of methane or bromomethanes (CH_3Br and CH_2Br_2).

To assess the carrier contribution to the product distribution over supported catalysts, CeO_2/MgO, CeO_2/Al_2O_3 and respective catalyst carriers MgO and Al_2O_3 were hence evaluated in methane and bromomethane oxidation under conditions closely matching those of MOB. In both cases, the rate of methane oxidation was negligible compared to the rate of bromomethanes oxidation (**Figure 12b**). Moreover, the activity of bulk and other supported CeO_2 catalysts in methane oxidation is *ca.* 2-8 times lower than the rate of methane oxidation. (**Figure S10**), while the rate of CH_2Br_2 oxidation is similar to or higher than the rate of oxybromination (**Figure 12a**). This indicates that a consecutive oxidation of bromomethanes has much higher impact on the formation of CO_x than the oxidation of methane. Still, in the case of bulk CeO_2 and CeO_2/ZrO_2

catalysts, the contribution of methane oxidation is likely higher compared to other materials. In agreement with the product distribution observed in oxybromination, MgO and CeO_2/MgO exhibited substantially lower activity for bromomethanes oxidation compared to Al_2O_3 and CeO_2/Al_2O_3. Notably, the rate of CH_2Br_2 oxidation over Al_2O_3 was rather high and comprised *ca*. 85% of the activity of CeO_2/Al_2O_3 catalyst in this reaction, in line with previous reports of the high activity of this carrier in the oxidation of halocarbons.[52,53] The latter involves halogen displacement by hydroxyl groups, whereby the eliminated hydrogen halides are prone to react with Lewis acidic aluminum atoms. This mechanism is consistent with our observations that CO is the main product in MOB, CH_3Br and CH_2Br_2 oxidation over both the CeO_2/Al_2O_3 catalyst and Al_2O_3 carrier, and with the increased surface Br:Ce ratio in the equilibrated CeO_2/Al_2O_3 catalyst (**Figure 5a**). Hence, a low selectivity to bromomethanes observed over CeO_2/Al_2O_3 catalyst is primarily caused by their combustion over the carrier (**Figure 11**).

Based on these results, CH_2Br_2 oxidation was chosen as a model reaction to assess the propensity of the other supported catalysts and carriers to combustion. Herein, ZrO_2 was also found to exhibit a relatively high activity (equivalent to *ca*. 20% of that of CeO_2/ZrO_2), which is in analogy to the Al_2O_3 carrier likely caused by the presence of basic OH groups and Lewis acidic zirconium ions.[54] In contrast, MgO, SiO_2, and SiC can be considered inert in CH_2Br_2 oxidation (**Figure 12c**). Nevertheless, CeO_2/SiO_2 and CeO_2/SiC catalysts were more active in combusting CH_2Br_2 than CeO_2/MgO, indicating that most CO_x formation (*ca*. 70-90%) over the former catalysts results from the enhanced oxidizing potential of the active phase (**Figure 5b**). Finally, a comparison of MOB, CH_4, CH_2Br_2, and HBr oxidation rates (**Figure 12a**), shows that CeO_2/MgO exhibits the lowest activity in CH_2Br_2 oxidation, while preserving relatively high activity in HBr oxidation and MOB, in good correspondence to the highest selectivity to bromocarbons observed over this catalysts (**Figure 6**). **Figure 12a** also demonstrates that catalyst must exhibit certain threshold activity in HBr oxidation in order to be sufficiently active in methane oxybromination. The clear example for this is CeO_2/Al_2O_3 catalyst, which shows the lowest rate of HBr oxidation (**Figure 12a**) and is consequentially the least active in oxybromination (**Figure 6**). On the other hand, the high activity in HBr oxidation (*e.g.*, bulk CeO_2 and CeO_2/ZrO_2) is correlated with the enhanced oxidation of bromomethanes. Therefore, a high oxybromination performance requires the balanced oxidizing potential, which is best-matched by CeO_2/MgO catalyst.

4. CONCLUSIONS

Supported CeO_2 catalysts were investigated in methane oxybromination, revealing major differences in performance compared to the bulk material, especially in the product distribution. The latter was strongly dependent on the type of carrier, which both influenced the dispersion, structure, and redox properties of the active phase, and exhibited a variable degree of inertness with respect to the oxidation of bromomethanes. Supported CeO_2 catalysts displayed decreased oxidizing potential compared to the bulk phase, which was associated with an enhanced selectivity due to a reduced activity in side combustion reactions (**Figure 11**). This effect was least pronounced over CeO_2/ZrO_2, which exhibited similar performance to bulk CeO_2. Another influential factor was the carrier propensity to combust bromomethanes. The latter reactions were more pronounced over the ZrO_2 and particularly the Al_2O_3 supports, which was related to the presence of Lewis acidic metal ions and basic hydroxyl groups, and resulted selectivity losses over the respective supported catalysts (**Figure 11**). An optimal balance of redox properties and carrier inertness was observed over CeO_2/MgO catalyst (**Figure 11**), stabilizing CeO_2 in the form of nanoparticles (*ca.* 9 nm). This catalytic system provided the highest selectivity to CH_3Br (61-81%), which substantially exceeded that of bulk CeO_2 (~ 40%) and rivalled those of the best previously reported oxybromination catalysts. Besides, the selectivity to CO_x (6-10%) was drastically reduced and its performance was stable for over 80 h on stream. Importantly, the product distribution over the MgO-supported catalysts was almost unaffected by the changes in the loading, size, and faceting of CeO_2 nanoparticles, which was in agreement with the similar oxidation potentials observed after equilibration of the latter catalysts, hinting at the adoption of a common surface structure. The findings are consistent with the mechanism comprising heterogeneous HBr oxidation into bromine, followed by the reaction of the latter with methane in the gas-phase. Thereby, supporting CeO_2 over suitable carriers provides an effective strategy to tailor its redox properties, and particularly the propensity to combustion, which is relevant in view of developing technical form catalyst for practical implementation of this technology.

ASSOCIATED CONTENT

Supporting Information. Supplementary information associated with this article, containing a scheme of reactor set-up, additional catalytic and characterization data, can be found in the online version.

AUTHOR INFORMATION

Corresponding Author

*Address: Institute for Chemical and Bioengineering, Department of Chemistry and Applied Biosciences, ETH Zurich, Vladimir-Prelog-Weg 1, CH-8093, Zurich, Switzerland. Phone: +41 44 633 7120. E-mail: jpr@chem.ethz.ch.

Author Contributions

The manuscript was written through contributions of all authors. All authors have given approval to the final version of the manuscript.

ACKNOWLEDGMENTS

This work was supported by ETH research grant (ETH-04 16-1) and by Swiss National Science Foundation (project no. 200021-156107). The authors acknowledge the Scientific Center for Optical and Electron Microscopy (ScopeM) of ETH Zurich for access to its facilities.

REFERENCES

(1) Tollefson, J. *Nature* **2016**, DOI:10.1038/nature.2016.19141.

(2) US Natural Gas Total Consumption. https://www.eia.gov/dnav/ng/hist/n9140us2a.htm (accessed September 6, 2017).

(3) Khalilpour, R.; Karimi, I. A. *Energy* **2012**, *40*, 317-328.

(4) McFarland, E. *Science* **2012**, *338*, 340-342.

(5) Horn, R.; Schlögl, R. *Catal. Lett.* **2015**, *145*, 23-39.

(6) Kondratenko, E. V.; Peppel, T.; Seeburg, D.; Kondratenko, V. A.; Kalevaru, N.; Martin, A.; Wohlrab, S. *Catal. Sci. Technol.* **2016**, *7*, 366-381.

(7) Lin, R.; Amrute, A. P.; Pérez-Ramírez, J. *Chem. Rev.* **2017**, *117*, 4182-4247.

(8) Ito, T.; Lunsford, J. H. *Nature* **1985**, *4*, 721-722.

(9) Zavyalova, U.; Holena, M.; Schlögl, R.; Baerns, M. *ChemCatChem* **2011**, *3*, 1935-1947.

(10) Galadima, A.; Muraza, O. *J. Ind. Eng. Chem.* **2015**, *37*, 1-13.

(11) Grundner, S.; Markovits, M. A. C.; Li, G.; Tromp, M.; Pidko, E. A.; Hensen, E. J. M.; Jentys, A.; Sanchez-Sanchez, M.; Lercher, J. A. *Nat. Commun.* **2015**, *6*, 7546.

(12) Tomkins, P.; Mansouri, A.; Bozbag, S. E.; Krumeich, F.; Park, M. B.; Alayon, E. M. C.; Ranocchiari, M.; van Bokhoven, J. A. *Angew. Chem. Int. Ed.* **2016**, *55*, 5467-5471.

(13) Guo, X.; Fang, G.; Li, G.; Ma, H.; Fan, H.; Yu, L.; Ma, C.; Wu, X.; Deng, D.; Wei, M.; Tan, D.; Si, R.; Zhang, S.; Li, J.; Sun, L.; Tang, Z.; Pan, X.; Bao, X. *Science* **2014**, *344*, 616-619.

(14) Dubey, A.; Kolekar, S. K.; Gopinath, C. S. *ChemCatChem* **2016**, *8*, 3650-3656.

(15) Lorkovic, I.; Noy, M.; Weiss, M.; Sherman, J.; McFarland, E.; Stucky, D.; Ford, P. C. *Chem. Commun.* **2004**, 566-567.

(16) Fong, H. L. H.; Swain, R. D. Integrated Process to Coproduce Aromatic Hydrocarbons and Ethylene and Propylene. U.S. Patent 2010/0234637 A1, September 16, 2010.

(17) Lorkovic, I. M.; Sun, S.; Gadewar, S.; Breed, A.; Macala, G. S.; Sardar, A.; Cross, S. E.; Sherman, J. H.; Stucky, G. D.; Ford, P. C. *J. Phys. Chem. A* **2006**, *110*, 8695-8700.

(18) Svelle, S.; Aravinthan, S.; Bjørgen, M.; Lillerud, K. P.; Kolboe, S.; Dahl, I. M.; Olsbye, U. *J. Catal.* **2006**, *241*, 243-254.

(19) He, J.; Xu, T.; Wang, Z.; Zhang, Q.; Deng, W.; Wang, Y. *Angew. Chem. Int. Ed.* **2012**, *51*, 2438-2442.

(20) Gas to Aromatics. http://www.gtctech.com/technology-licensing/gas-to-aromatics (accessed September 6, 2017).

(21) Moser, M.; Rodríguez-García, L.; Amrute, A. P.; Pérez-Ramírez, J. *ChemCatChem* **2013**, *5*, 3520-3523.

(22) Paunović, V.; Zichittella, G.; Moser, M.; Amrute, A. P.; Pérez-Ramírez, J. *Nat. Chem.* **2016**, *8*, 803-809.

(23) Zichittella, G.; Paunović, V.; Amrute, A. P.; Pérez-Ramírez, J. *ACS Catal.* **2017**, *7*, 1805-1817.

(24) Paunović, V.; Lin, R.; Scharfe, M.; Amrute, A. P.; Mitchell, S.; Hauert, R.; Pérez-Ramírez, J. *Angew. Chem. Int. Ed.* **2017**, *56*, 9791-9795.

(25) Ding, K.; Derk, A. R.; Zhang, A.; Hu, Z.; Stoimenov, P.; Stucky, G. D.; Metiu, H.; McFarland, E. W. *ACS Catal.* **2012**, 479-486.

(26) Trovarelli, A. *Catal. Rev. Sci. Eng.* **1996**, *38*, 439-520.

(27) Montini, T.; Melchionna, M.; Monai, M.; Fornasiero, P. *Chem. Rev.* **2016**, *116*, 5987-6041.

(28) Amrute, A. P.; Mondelli, C.; Moser, M.; Novell-Leruth, G.; López, N.; Rosenthal, D.; Farra, R.; Schuster, M. E.; Teschner, D.; Schmidt, T.; Pérez-Ramírez, J. *J. Catal.* **2012**, *286*, 287-297.

(29) Möller, M.; Urban, S.; Cop, P.; Weller, T.; Ellinghaus, R.; Kleine-Boymann, M.; Fiedler, C.; Sann, J.; Janek, J.; Chen, L.; Klar, P. J.; Hofmann, D. M.; Philipps, J.; Dolcet, P.; Gross, S.; Over, H.; Smarsly, B. M. *ChemCatChem* **2015**, *7*, 3738-3747.

(30) Mai, H.-X.; Sun, L.-D.; Zhang, Y.-W.; Si, R.; Feng, W.; Zhang, H.-P.; Liu, H.-C.; Yan, C.-H. *J. Phys. Chem. B* **2005**, *109*, 24380-24385.

(31) Wu, Z.; Li, M.; Overbury, S. H. *J. Catal.* **2012**, *285*, 61-73.

(32) Torrente-Murciano, L.; Gilbank, A.; Puertolas, B.; Garcia, T.; Solsona, B.; Chadwick, D. *Appl. Catal., B* **2013**, *132-133*, 116-122.

(33) Trovarelli, A.; Llorca, J. *ACS Catal.* **2017**, *7*, 4716-4735.

(34) Sun, C.; Li, H.; Chen, L. *Energy Environ. Sci.* **2012**, *5*, 8475-8505.

(35) Fernández-García, M.; Martínez-Arias, A.; Iglesias-Juez, A.; Belver, C.; Hungría, A. B.; Conesa, J. C.; Soria, J. *J. Catal.* **2000**, *194*, 385-392.

(36) Trovarelli, A.; Boaro, M.; Rocchini, E.; de Leitenburg, C.; Dolcetti, G. *J. Alloys Compd.* **2001**, *33*, 584-591.

(37) Reddy, B. M.; Khan, A.; Lakshmanan, P.; Aouine, M.; Loridant, S.; Volta, J. C. *J. Phys. Chem. B* **2005**, *109*, 3355-3363.

(38) Reddy, B. M.; Lakshmanan, P.; Bharali, P.; Saikia, P. *J. Phys. Chem. C* **2007**, *111*, 10478-10483.

(39) Park, J. B.; Graciani, J.; Evans, J.; Stacchiola, D.; Ma, S.; Liu, P.; Nambu, A.; Sanz, J. F.; Hrbek, J.; Rodriguez, J. A. *Proc. Natl. Acad. Sci.* **2009**, *106*, 4975-4980.

(40) Strunk, J.; Vining, W. C.; Bell, A. T. *J. Phys. Chem. C* **2011**, *115*, 4114-4126.

(41) Moser, M.; Mondelli, C.; Schmidt, T.; Girgsdies, F.; Schuster, M. E.; Farra, R.; Szentmiklósi, L.; Teschner, D.; Pérez-Ramírez, J. *Appl. Catal., B* **2013**, *132-133*, 123-131.

(42) Tinoco, M.; Sanchez, J. J.; Yeste, M. P.; Lopez-Haro, M.; Trasobares, S.; Hungria, A. B.; Bayle-Guillemaud, P.; Blanco, G.; Pintado, J. M.; Calvino, J. J. *ChemCatChem* **2015**, *7*, 3763-3778.

(43) Carberry, J. J. Physico-Chemical Aspects of Mass and Heat Transfer in Heterogeneous Catalysis. In *Catalysis Science and Technology*; Anderson, J. R., Boudart, M., Eds.; Springer-Verlag, Berlin, Heidelberg 1987; Vol. 8, pp 131-172.

(44) Mears, D. E. *J. Catal.* **1971**, *20*, 127-131.

(45) Wu, Z.; Li, M.; Howe, J.; Meyer, H. M.; Overbury, S. H. *Langmuir* **2010**, *26*, 16595–16606.

(46) Trovarelli, A.; Zamar, F.; Llorca, J.; de Leitenburg, C.; Dolcetti, G.; Kiss, J. T. *J. Catal.* **1997**, *169*, 490-502.

(47) Shyu, J. Z.; Weber, W. H.; Gandhi, H. S. *J. Phys. Chem.* **1988**, *92*, 4964-4970.

(48) Inoue, Y.; Nakashima, S.; Mitsuishi, A.; Tabata, S.; Tsuboi, S. *Solid State Commun.* **1983**, *48*, 1071-1075.

(49) Mullins, D. R. *Surf. Sci. Rep.* **2015**, *70*, 42-85.

(50) Rocchini, E.; Trovarelli, A.; Llorca, J.; Graham, G. W.; Weber, W. H.; Maciejewski, M.; Baiker, A. *J. Catal.* **2000**, *194*, 461-478.

(51) Kistiakowsky, G. B.; Van Artsdalen, E. R. *J. Chem. Phys.* **1944**, *12*, 469-478.

(52) Dai, Q.; Robinson, G. N.; Freedman, A. *J. Phys. Chem. B* **1997**, *101*, 4940-4946.

(53) van den Brink, R. W.; Mulder, P.; Louw, R.; Sinquin, G.; Petit, C.; Hindermann, J.-P. *J. Catal.* **1998**, *180*, 153-160.

(54) Pokrovski, K.; Jung, K. T.; Bell, A. T. *Langmuir* **2001**, *17*, 4297-4303.

Table 1. Conditions applied in the reactions studied.

Reaction	W_{cat} / g	F_T / cm^3 min^{-1}	Feed composition[a] / mol.%					
			CH_4	HBr	CO	CH_3Br	CH_2Br_2	O_2
CH_4 oxybromination	1.0	100-200	3-20	3-12	0	0	3	1.5-6
CH_4 oxidation	1.0	100	6	0	0	0	3	3
CH_3Br oxidation	0.2	100	0	0	0	1	0	2
CH_2Br_2 oxidation	0.2	100	0	0	0	0	1	2
CO oxidation	0.2	100	6	0	1.5	0	0	3
HBr oxidation	0.5	100	0	6	0	0	0	3

[a] Ar (4.5 mol.%) was added as an internal standard to all the reaction mixtures, except for HBr oxidation. He was used as the balance gas.

Table 2. Characterization data of the samples.

Catalyst	CeO_2 nominal / wt.%	CeO_2 bulk[a] / wt.%		CeO_2 crystallite size[b] / nm		CeO_2 crystallite size[c] / nm		S_{BET}[d] / $m^2\ g^{-1}$			V_{pore}[e] / $cm^3\ g^{-1}$		
		fresh	used	fresh	used	fresh	used	support	fresh	used	support	fresh	used
CeO_2	100	-	-	20	21	-	-	-	49	38		0.13	0.11
CeO_2/ZrO_2	2	2.1	2.1	-	-	-	-	41	41	41	0.27	0.07	0.06
CeO_2/Al_2O_3	2	2.0	2.0	-	-	-	-	143	143	146	0.51	0.51	0.50
CeO_2/SiC	2	2.0	2.0	9	9	9	9	36	38	36	0.10	0.29	0.28
CeO_2/SiO_2	2	1.9	1.9	5	5	4	3	241	246	246	1.90	1.25	1.23
CeO_2/MgO	2	2.0	2.0	9	9	6	6	29	27	27	0.22	0.19	0.21
CeO_2/MgO-0.5	0.5	0.6	0.5	-	-	6	6	29	48	30	0.22	0.19	0.19
CeO_2/MgO-0.1	0.1	0.1	0.1	-	-	-	-	29	37	26	0.22	0.21	0.19
CeO_2/MgO-0.5-973	0.5	0.6	0.6	6	7	6	6	28	24	22	0.14	0.14	0.15
CeO_2/MgO-0.5-1173	0.5	0.6	0.6	10	10	-	-	28	24	21	0.14	0.12	0.15
CeO_2/MgO-0.5-1373	0.5	0.5	0.5	16	16	-	18	28	22	18	0.14	0.20	0.15
CeO_2/MgO-m	2	2.0	1.9	7	7	-	-	29	32	25	29	0.20	0.19
CeO_2/MgO-c	2	2.1	1.9	7	7	-	9	-	48	29	-	0.16	0.14
CeO_2/MgO-h	2	1.9	2.4	16	16	-	10	29	50	32	29	0.20	0.14

[a] ICP-OES. [b] Scherrer equation. [c] STEM. [d] BET model. [e] Volume of N_2 adsorbed at $p/p_0 = 0.98$.

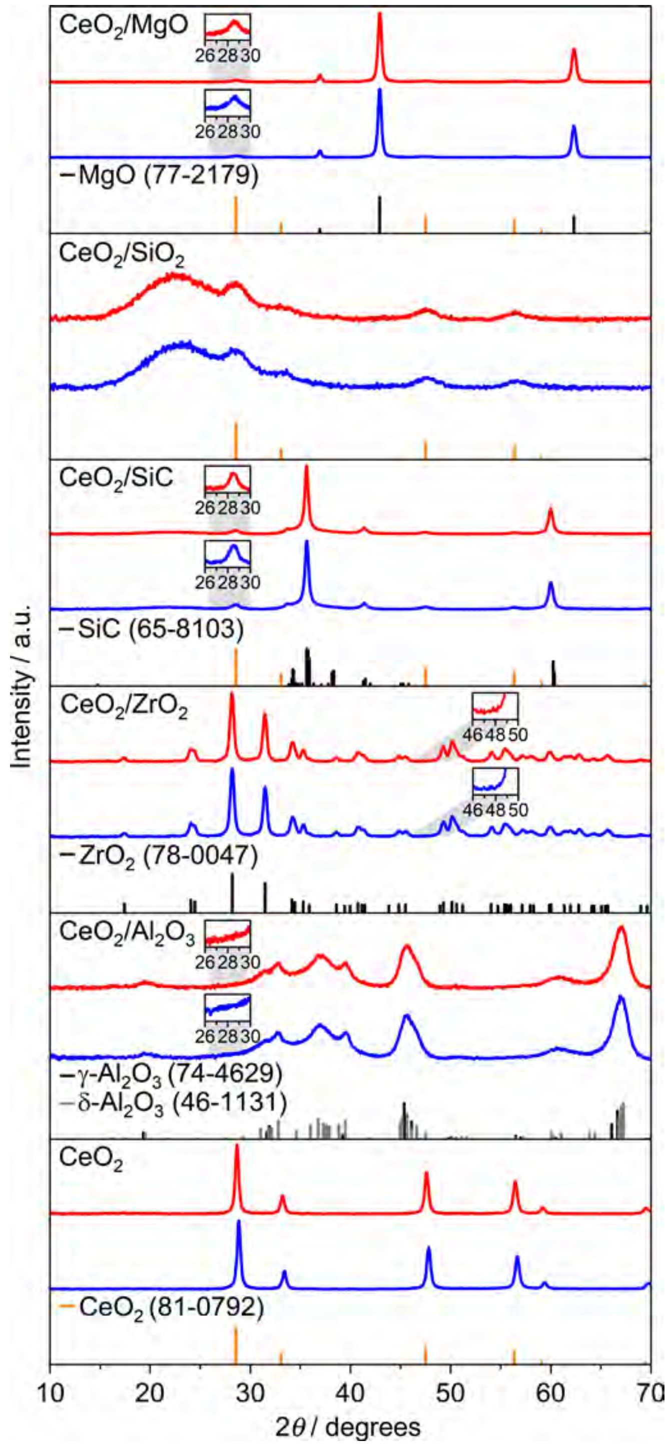

Figure 1. XRD patterns of bulk and supported CeO_2 catalysts in fresh form (blue) and after equilibration in methane oxybromination (red). Reference patterns are shown as vertical lines below the measured diffractograms and are identified with their ICDD-PDF numbers. The insets

show magnification of the 2θ regions where the main CeO_2 reflections are expected. Equilibration conditions: CH_4:HBr:O_2:Ar:He = 6:6:3:4.5:80.5, F_T/W_{cat} = 100 cm^3 min^{-1} g_{cat}^{-1}, T = 773 K, P = 1 bar, *tos* = 5h.

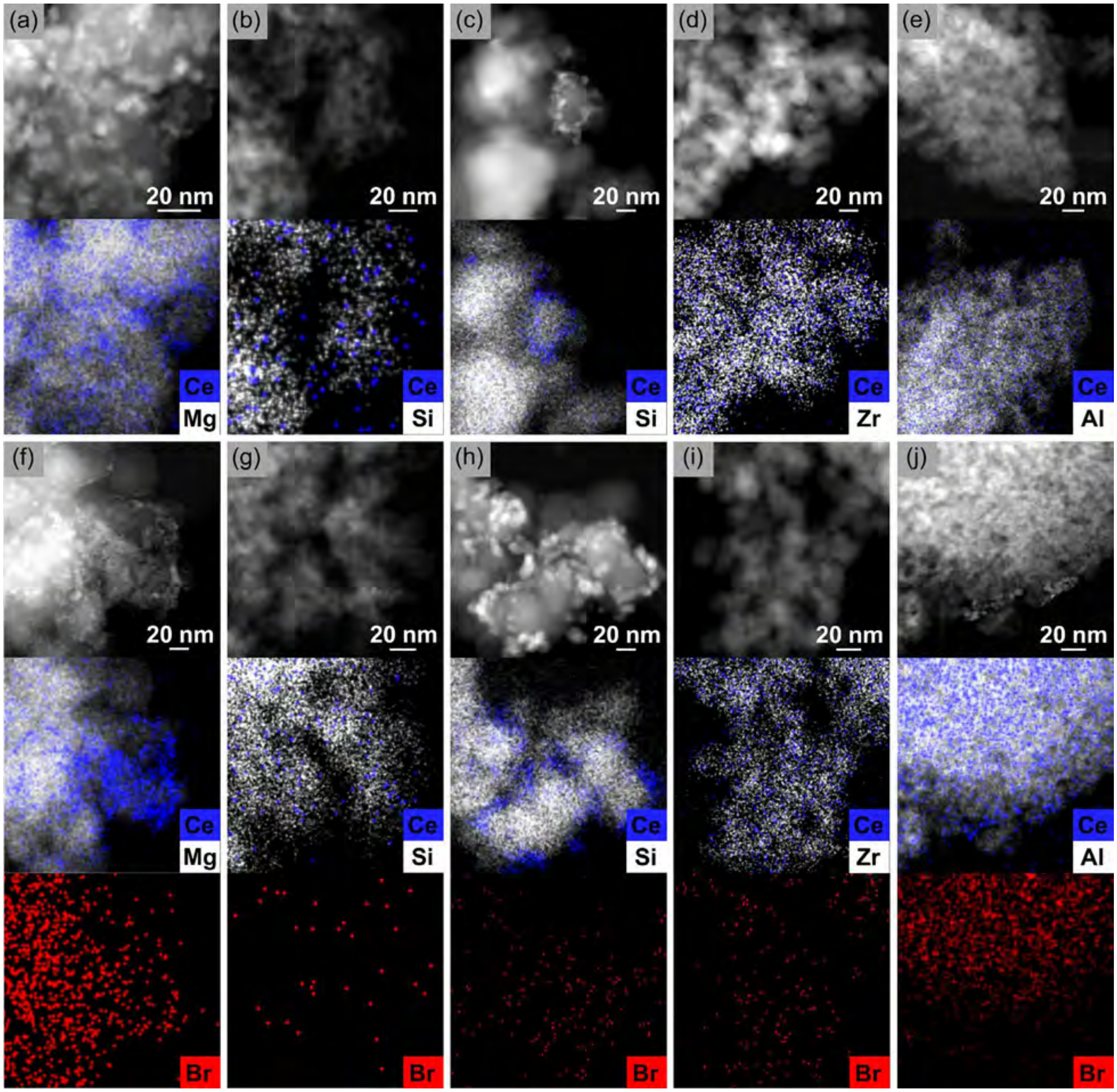

Figure 2. HAADF-STEM micrographs and corresponding elemental maps of (a,f) CeO_2/MgO, (b,g) CeO_2/SiO_2, (c,h) CeO_2/SiC, (d,i) CeO_2/ZrO_2, and (e,j) CeO_2/Al_2O_3 catalysts in fresh form (a-e) and after equilibration in methane oxybromination (f-j). Equilibration conditions as reported in the caption of **Figure 1**.

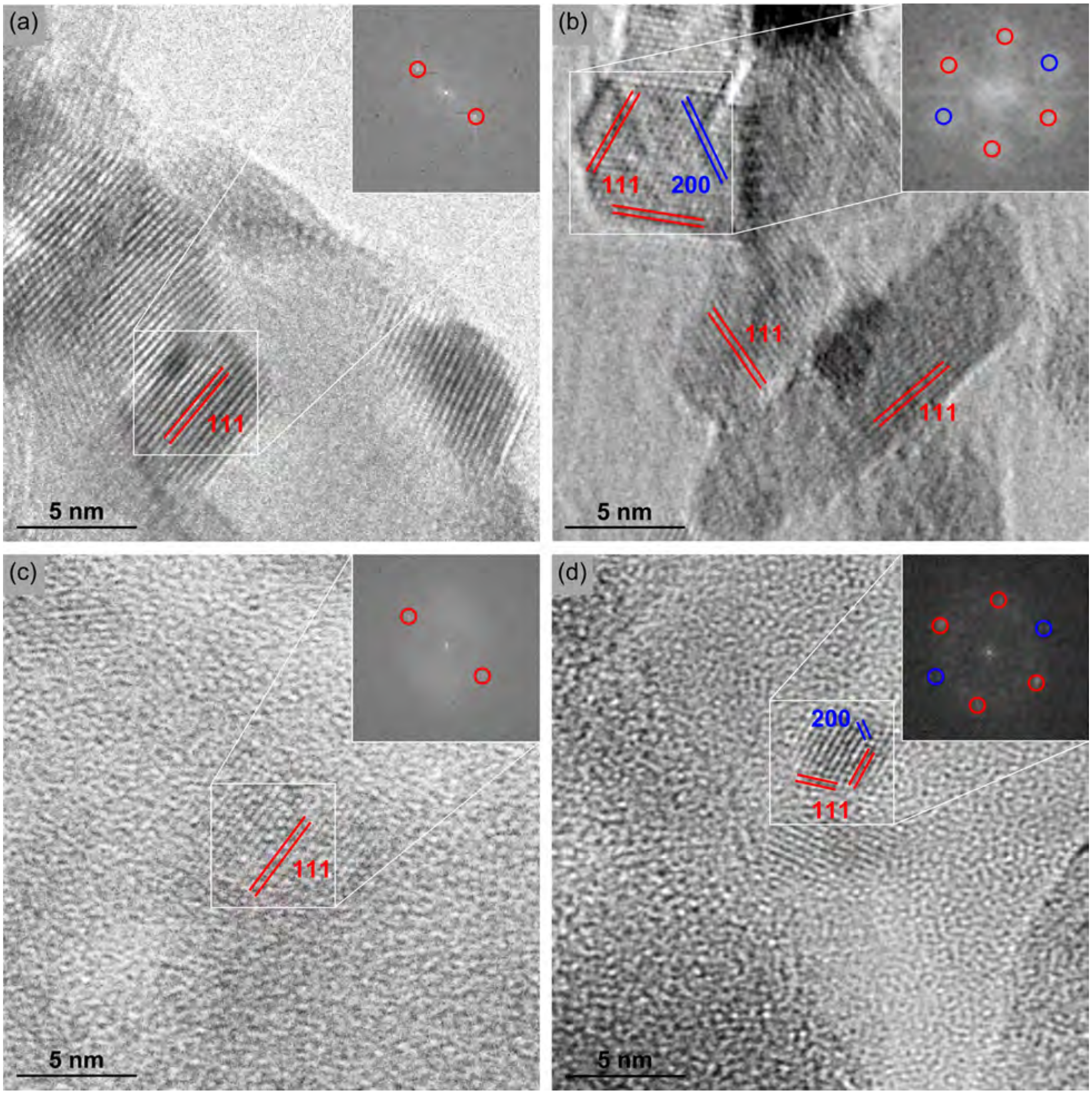

Figure 3. HRTEM micrographs of (a,b) CeO_2/MgO and (c,d) CeO_2/SiO_2 catalysts in fresh form (a,c) and after equilibration in methane oxybromination (b,d). The insets show the fast Fourier transform of the boxed regions. Equilibration conditions as reported in the caption of **Figure 1**.

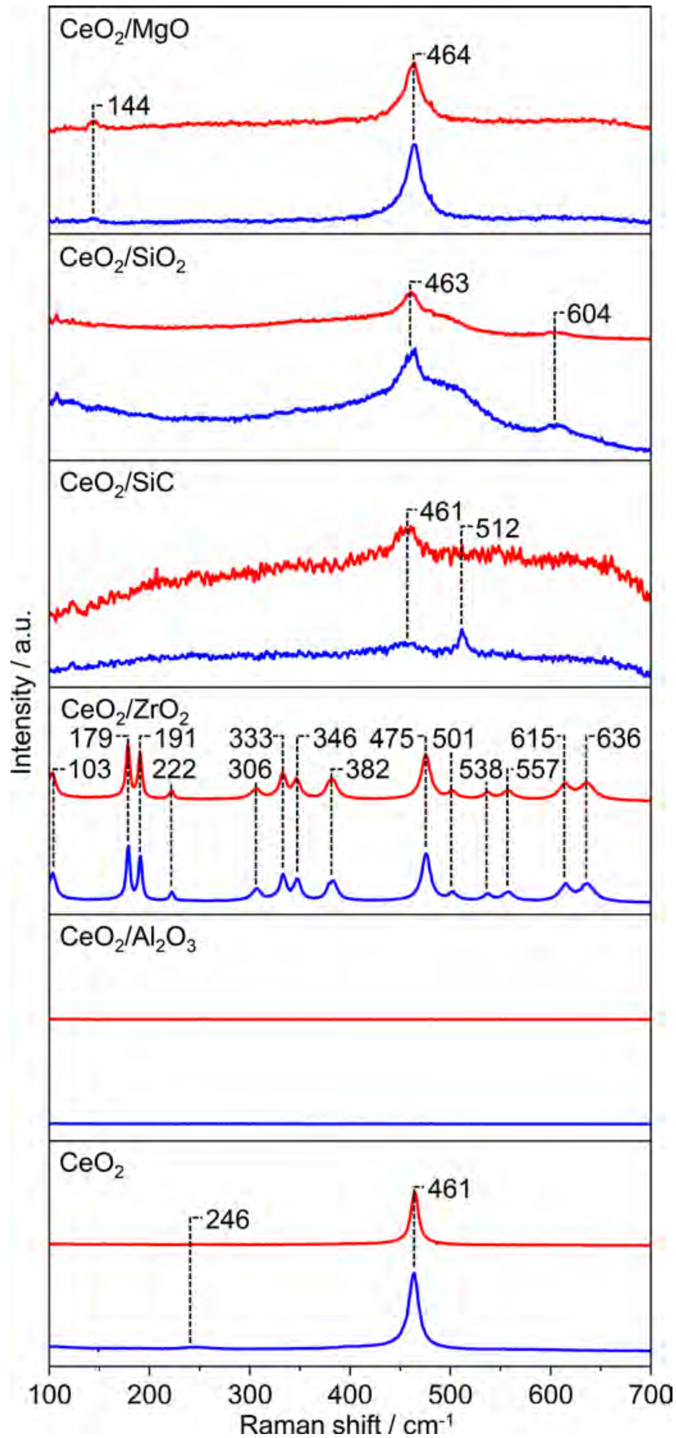

Figure 4. Raman spectra of bulk and supported CeO_2 catalysts in fresh form (blue) and after equilibration in methane oxybromination (red). Equilibration conditions as reported in the caption of **Figure 1**.

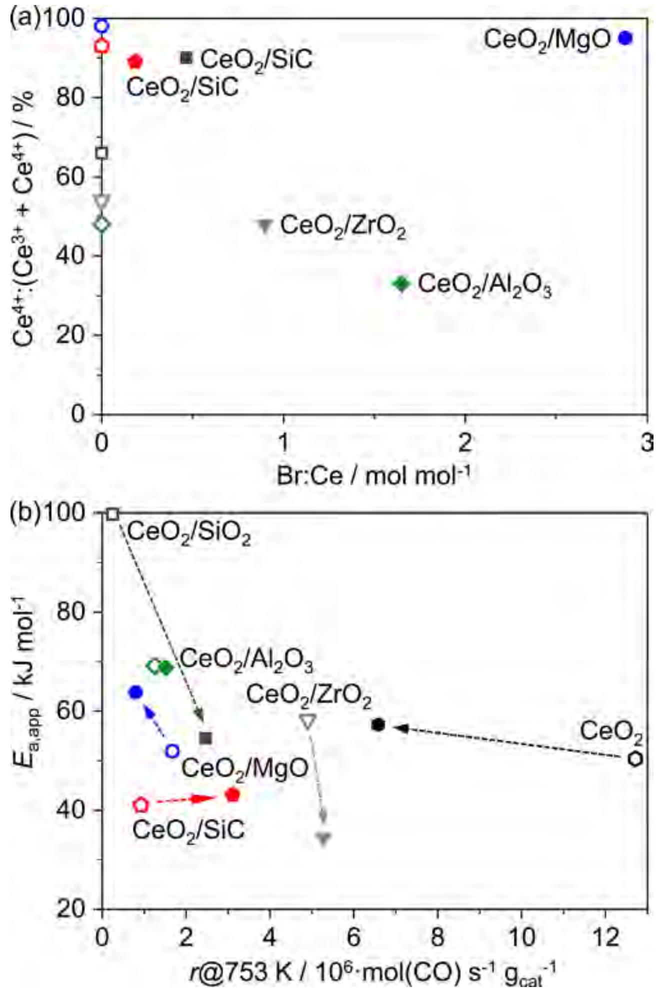

Figure 5. (a) The fraction of Ce^{4+} *versus* the Br:Ce atomic ratio determined by XPS, and (b) a comparison of the apparent activation energy, $E_{a,app}$, and the rate of CO oxidation at 753 K, *r*@753 K, for the bulk and supported CeO_2 catalysts in fresh form (open symbols) and after equilibration in methane oxybromination (solid symbols). Equilibration conditions as reported in the caption of **Figure 1**. Conditions in CO oxidation: CO:O_2:Ar:He = 1.5:3:4.5:91, F_T/W_{cat} = 500 cm^3 min^{-1} g_{cat}^{-1}, P = 1 bar.

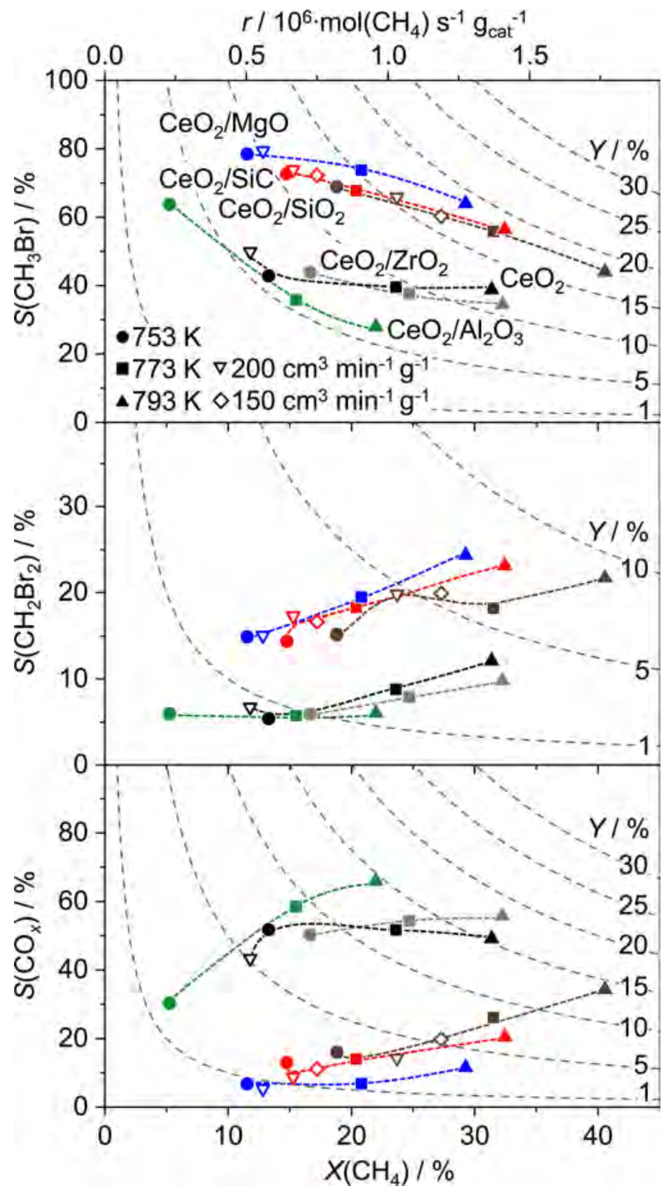

Figure 6. Selectivity to CH_3Br (top), CH_2Br_2 (middle), and CO_x (bottom) *versus* the conversion in methane oxybromination over bulk and supported CeO_2 catalysts at various temperatures (solid symbols, $F_T/W_{cat} = 100$ cm^3 min^{-1} g$_{cat}^{-1}$) and space velocities ($T = 773$ K, open symbols). The dashed gray lines indicate the yields of respective products. Conditions: CH_4:HBr:O_2:Ar:He = 6:6:3:4.5:80.5, $P = 1$ bar.

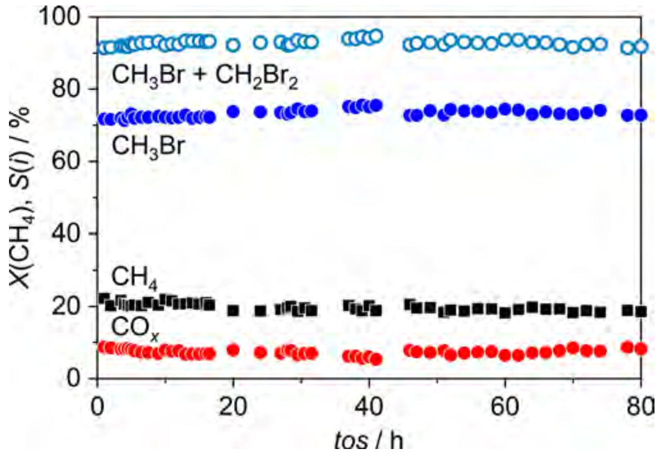

Figure 7. Conversion and product selectivity *versus* time-on-stream, in methane oxybromination over CeO_2/MgO catalyst. Conditions: CH_4:HBr:O_2:Ar:He = 6:6:2:4.5:81.5, F_T/W_{cat} = 100 cm^3 min^{-1} g$_{cat}$$^{-1}$, T = 773 K, P = 1 bar.

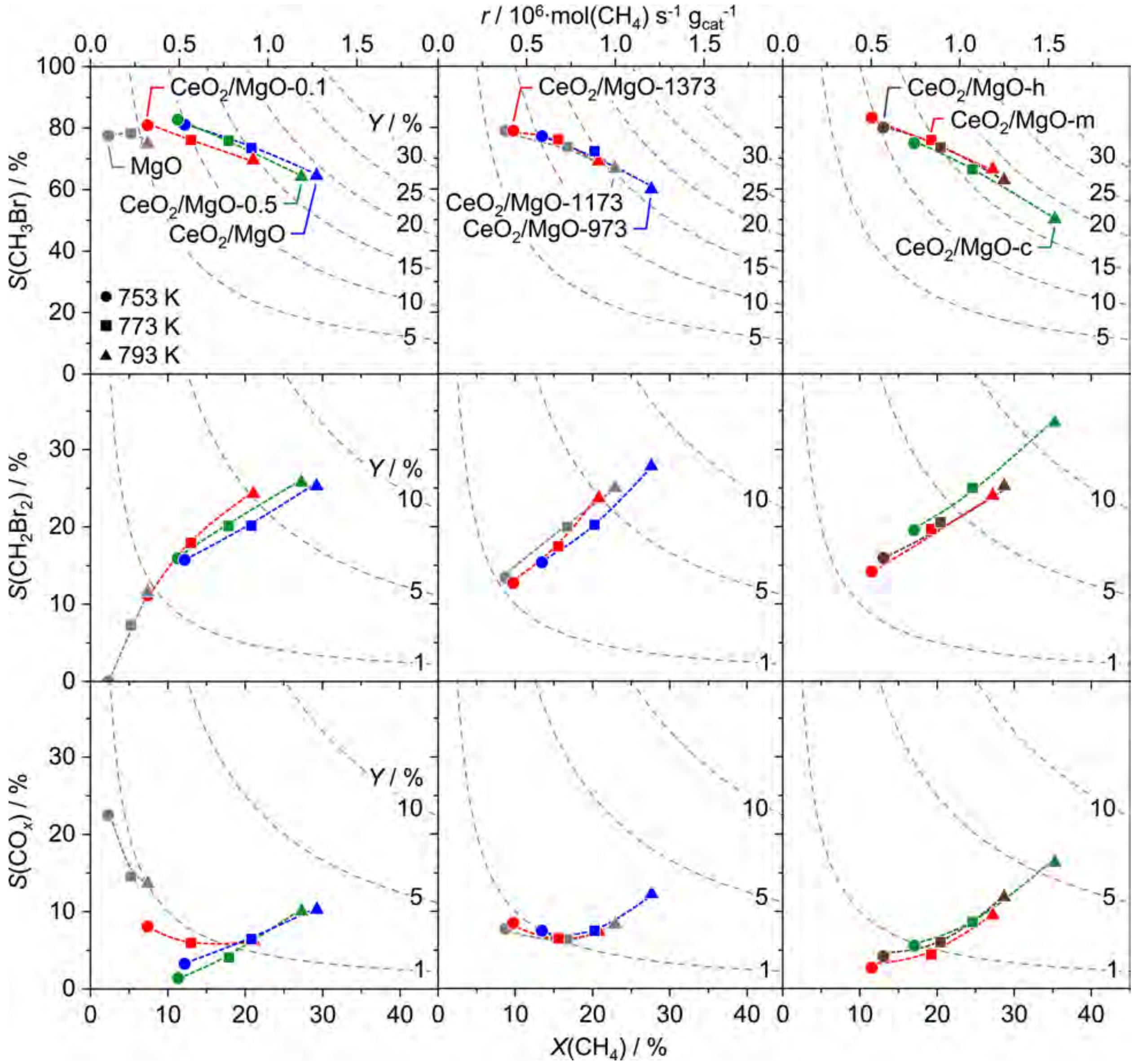

Figure 8. Selectivity to CH_3Br (top), CH_2Br_2 (middle), and CO_x (bottom) *versus* the conversion in methane oxybromination over MgO-supported CeO_2 catalysts prepared using different loading (left), calcination temperature (middle), and synthesis method (right) at various temperatures. The dashed gray lines indicate the yields of respective products. Conditions: CH_4:HBr:O_2:Ar:He = 6:6:3:4.5:80.5, F_T/W_{cat} = 100 cm^3 min^{-1} g$_{cat}$$^{-1}$, P = 1 bar.

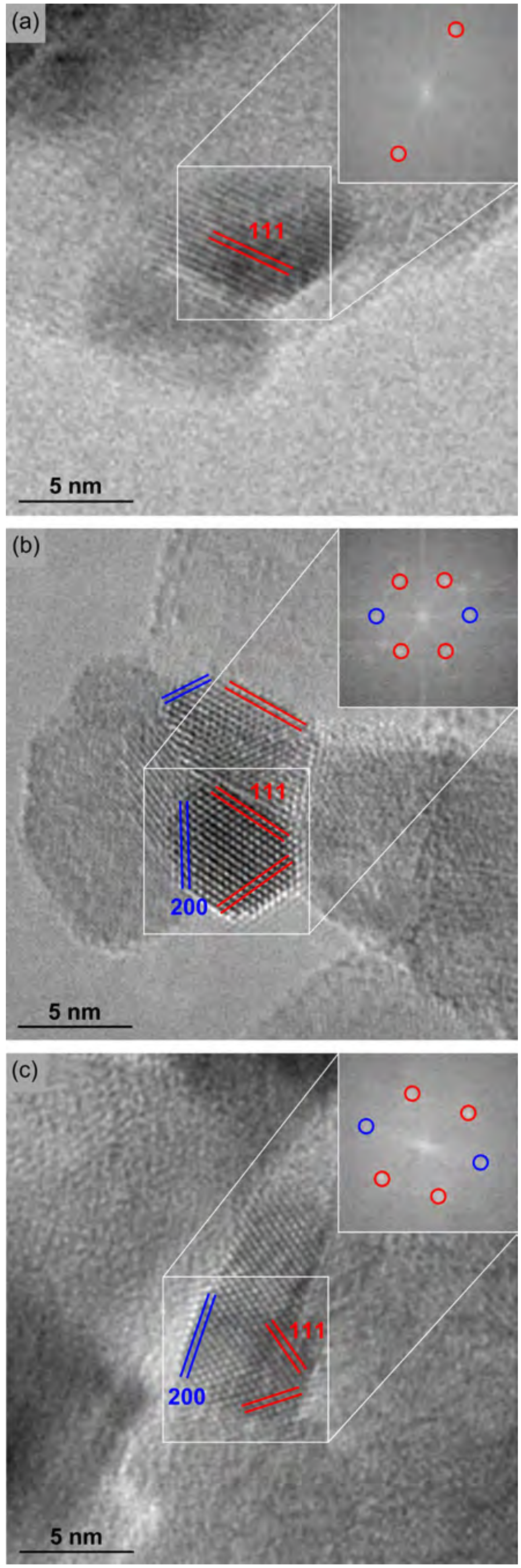
(a)
111
5 nm
(b)
111
200
5 nm
(c)
111
200
5 nm

Figure 9. HRTEM micrographs of (a) CeO_2/MgO-0.5, (b) CeO_2/MgO-c, and (c) CeO_2/MgO-h catalysts equilibrated under methane oxybromination. The insets show the fast Fourier transform of the boxed regions. Equilibration conditions as reported in the caption of **Figure 1**.

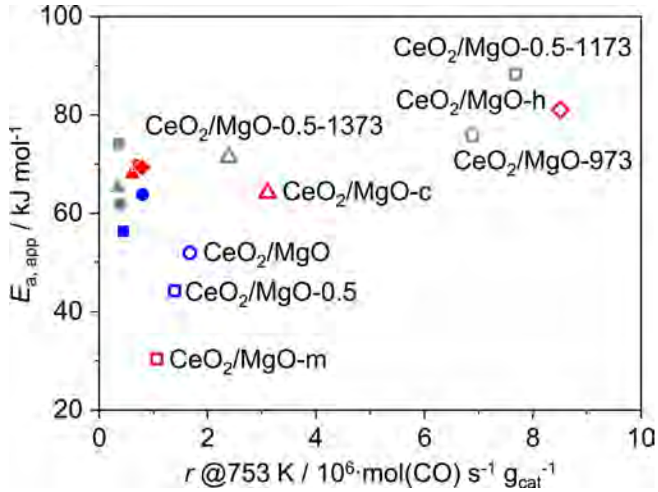

Figure 10. A comparison of the apparent activation energy and the rate of CO oxidation at 753 K for MgO-supported CeO_2 catalysts in fresh form (open symbols) and after equilibration in methane oxybromination (solid symbols). Conditions: $CO:O_2:Ar:He = 1.5:3:4.5:91$, $F_T/W_{cat} = 500\ cm^3\ min^{-1}\ g_{cat}^{-1}$, $P = 1$ bar. Equilibration conditions as reported in the caption of **Figure 1**.

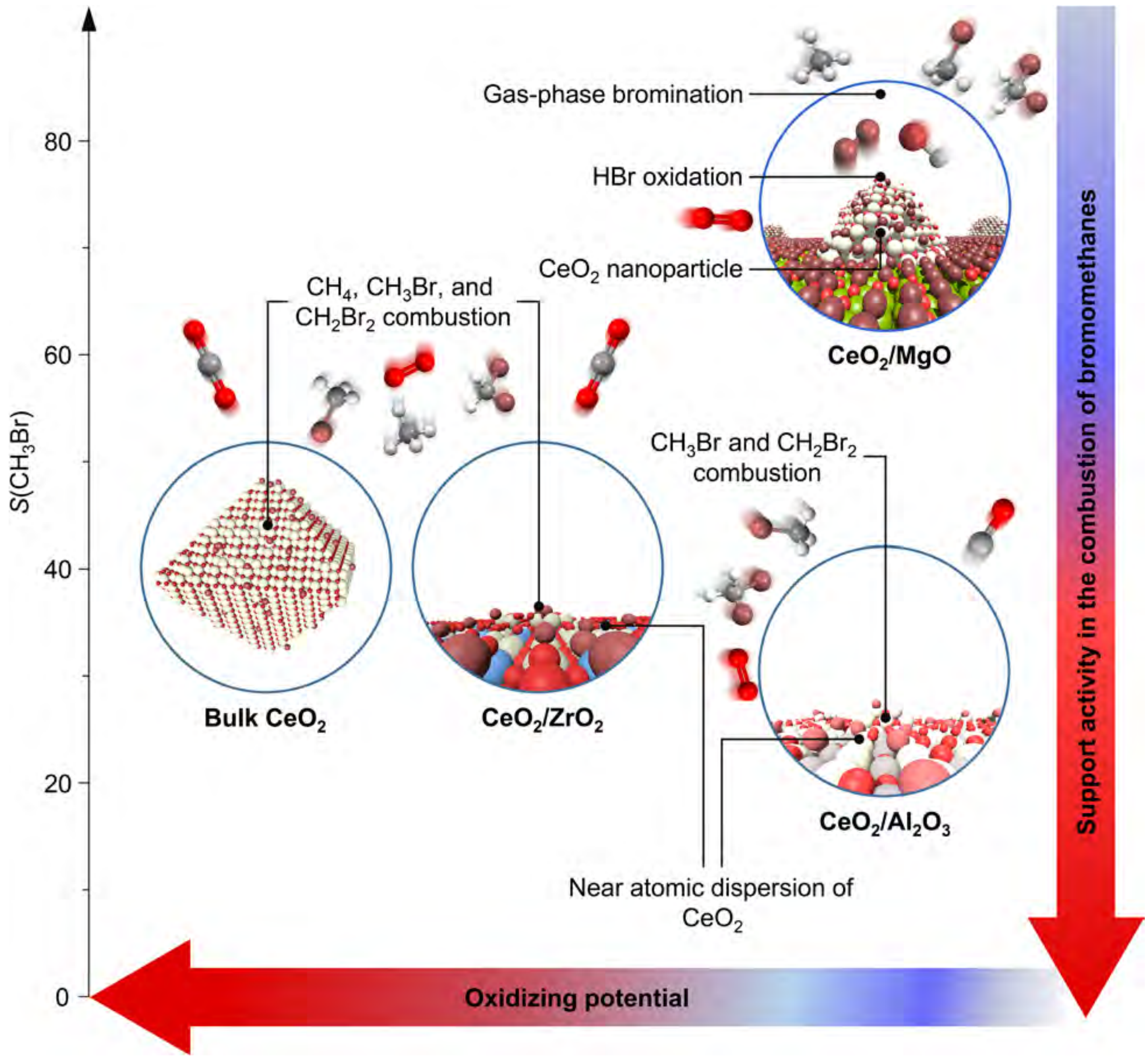

Figure 11. Criteria for the design of supported CeO_2 catalyst for methane oxybromination and schematic representation of key parts of the reaction scheme.

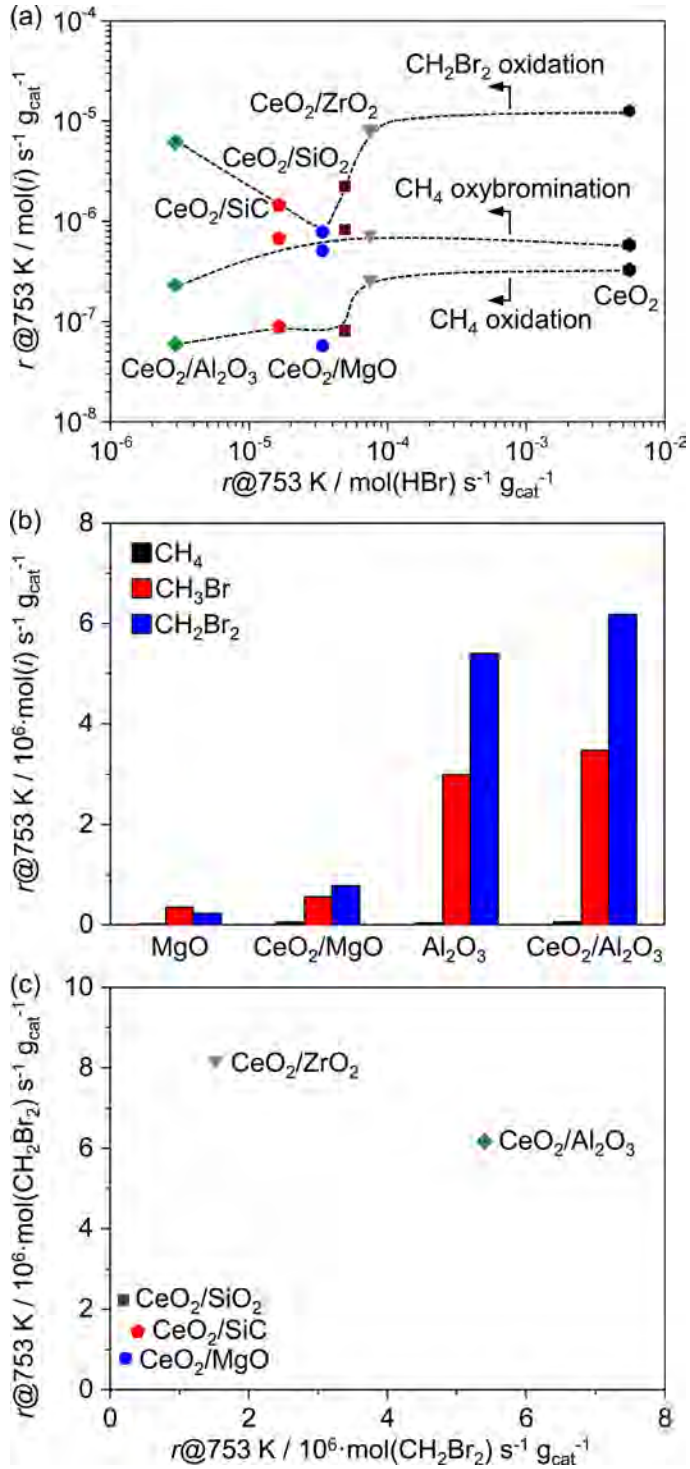

Figure 12. (a) Rates of methane oxybromination, methane and CH_2Br_2 oxidation *versus* the rate of HBr oxidation at 753 K over the bulk and supported CeO_2 catalysts. (b) Rates of methane, CH_3Br, and CH_2Br_2 oxidation at 753 K over the bare MgO and Al_2O_3 supports and the supported

CeO_2/MgO and CeO_2/Al_2O_3 catalysts. (c) Rate of CH_2Br_2 oxidation over the supported CeO_2 catalysts *versus* the rate of CH_2Br_2 oxidation over respective bare supports after equilibration in methane oxybromination. The oxidation of CH_3Br (CH_3Br:O_2:Ar:He = 1:2:4.5:92.5) and CH_2Br_2 (CH_2Br_2:O_2:Ar:He = 1:2:4.5:92.5) were performed at F_T/W_{cat} = 500 $cm^3\ min^{-1}\ g_{cat}^{-1}$, and the oxidation of HBr (HBr:O_2:He = 6:3:91) and methane (CH_4:O_2:Ar:He = 6:3:4.5:86.5) were studied at F_T/W_{cat} = 200 $cm^3\ min^{-1}\ g_{cat}^{-1}$ and F_T/W_{cat} = 100 $cm^3\ min^{-1}\ g_{cat}^{-1}$, respectively. Methane oxybromination was performed under the conditions reported in the caption of **Figure 6**. All tests were conducted at P = 1 bar.

Table of Contents Graphic

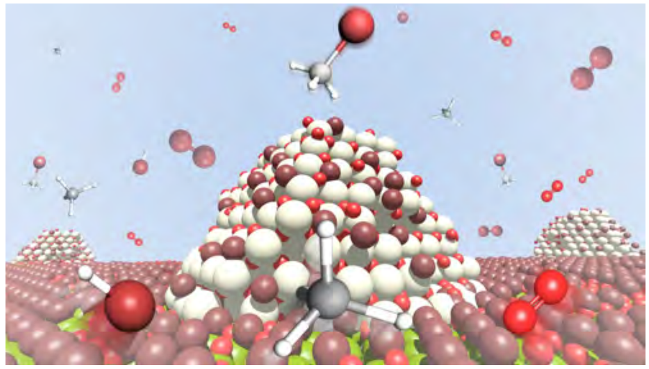

Supporting Information

Selective Methane Oxybromination over Nanostructured Ceria Catalysts

Vladimir Paunović,[†] Guido Zichittella,[†] Sharon Mitchell,[†] Roland Hauert,[§] and Javier Pérez-Ramírez*,[†]

[†] Institute for Chemical and Bioengineering, Department of Chemistry and Applied Biosciences, ETH Zurich, Vladimir-Prelog-Weg 1, CH-8093 Zurich, Switzerland

[§] EMPA, Swiss Federal Laboratories for Materials Science and Technology, Überlandstrasse 129, CH-8600 Dübendorf, Switzerland

* Corresponding author. E-mail: jpr@chem.ethz.ch

Table S1. Assessment of the intraparticle mass transfer limitations in methane oxybromination over supported ceria catalysts.[a]

Catalyst	d_p / mm	X / %	S / %		
		CH_4	CH_3Br	CH_3Br	CO_x
CeO_2/MgO	0.075-0.0125	21	72	22	6
CeO_2/MgO	0.2-0.3	21	73	21	6
CeO_2/MgO	0.4-0.6	21	74	19	7
CeO_2/SiO_2	0.075-0.0125	31	57	18	25
CeO_2/SiO_2	0.4-0.6	31.5	56	18	26

[a] Conditions: CH_4:HBr:O_2:Ar:He = 6:6:3:4.5:80.5, F_T/W_{cat} = 100 cm^3 min^{-1} g_{cat}^{-1}, T = 773 K, P = 1 bar.

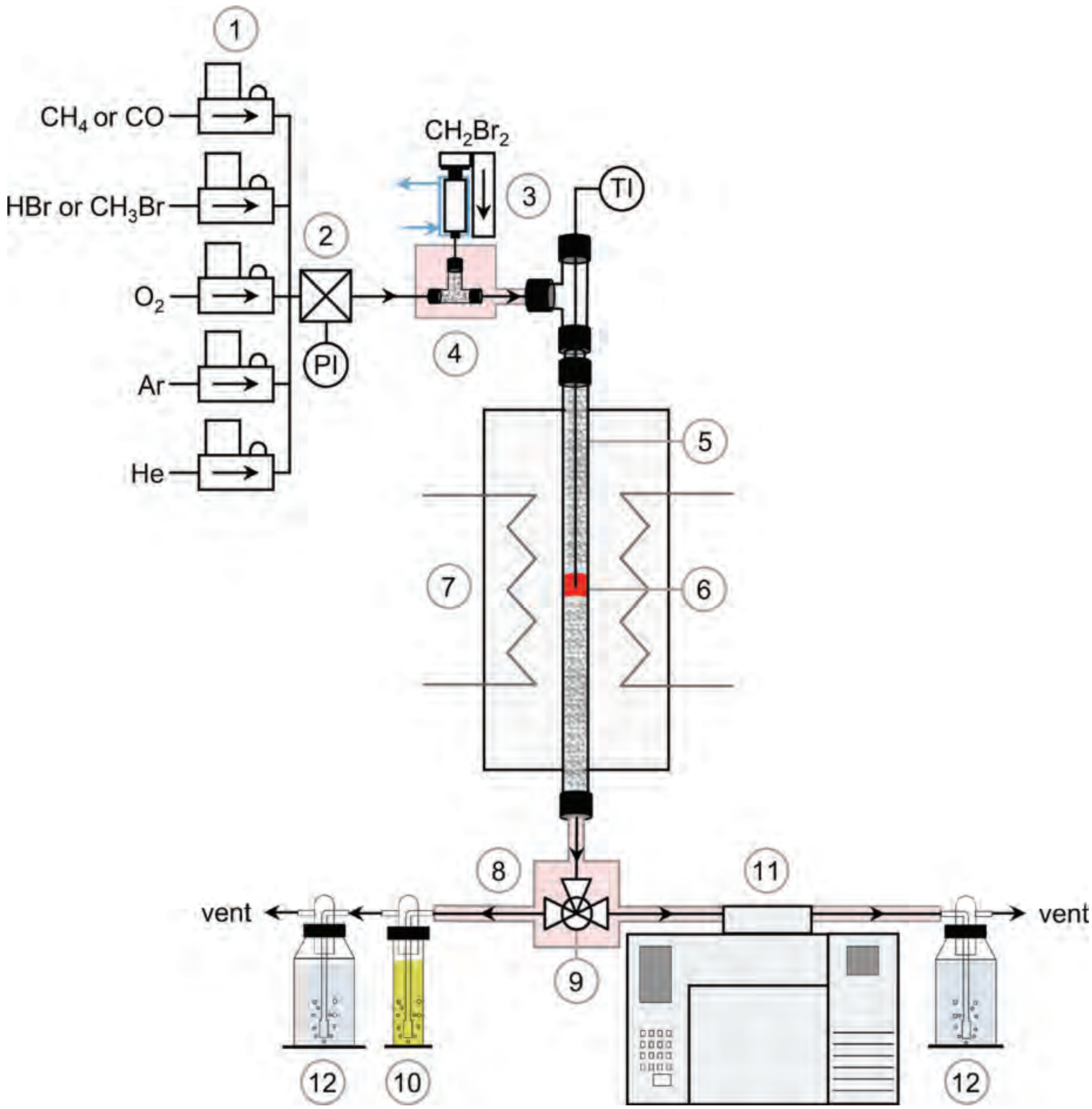

Figure S1. Flowsheet of the laboratory setup used for the continuous-flow methane oxybromination, and oxidation of CO, CH_3Br, CH_2Br_2, and HBr. 1: mass flow controllers, 2: gas mixer, 3: syringe pump with water-cooling system, 4: vaporizer, 5: quartz reactor, 6: catalyst bed, 7: oven, 8: heat tracing (pink), 9: three-way sampling valve, 10: KI impinging bottle, 11: GC-MS, 12: NaOH impinging bottles, PI: pressure indicator, and TI: temperature indicator.

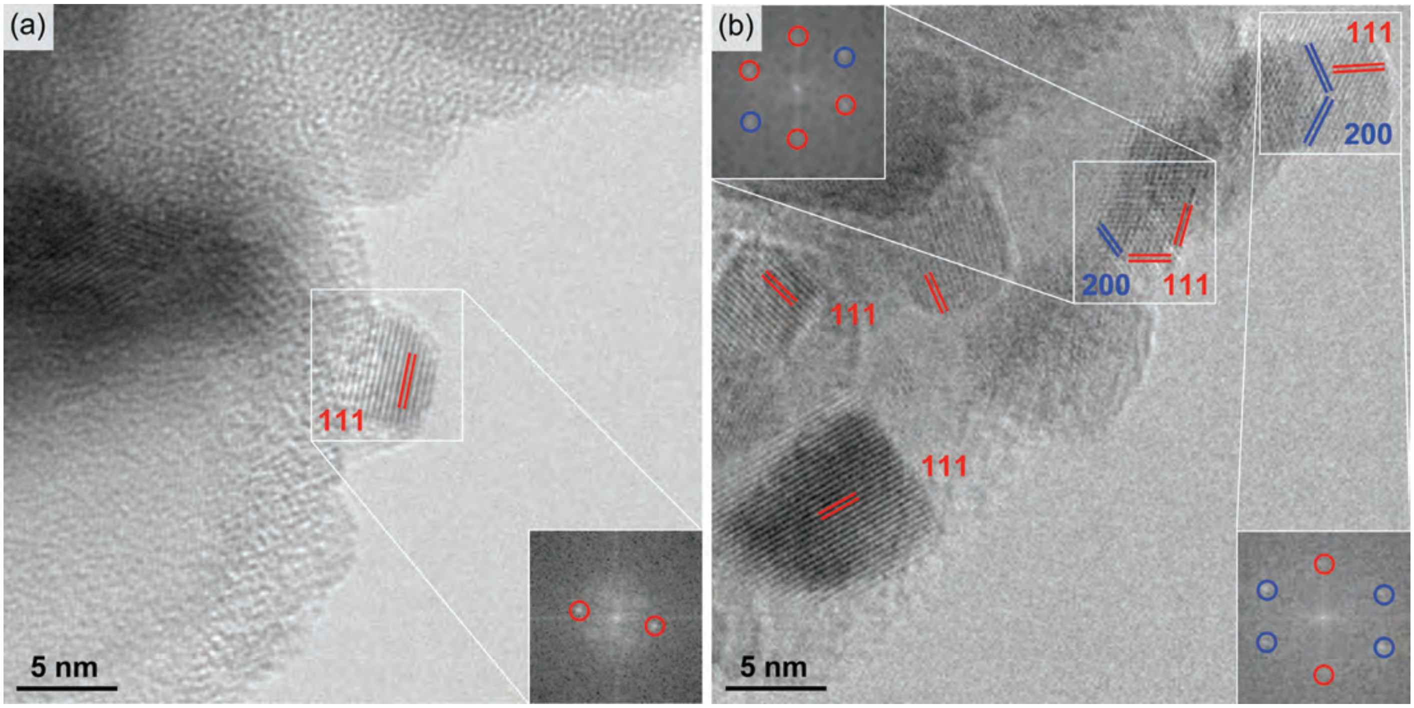

Figure S2. HRTEM micrographs of (a) fresh CeO_2/SiC and (b) CeO_2/MgO after equilibration in methane oxybromination. The insets show the fast Fourier transform of the boxed regions Equilibration conditions: CH_4:HBr:O_2:Ar:He = 6:6:3:4.5:80.5, F_T/W_{cat} = 100 cm^3 min^{-1} g$_{cat}^{-1}$, T = 773 K, P = 1 bar, *tos* = 5h.

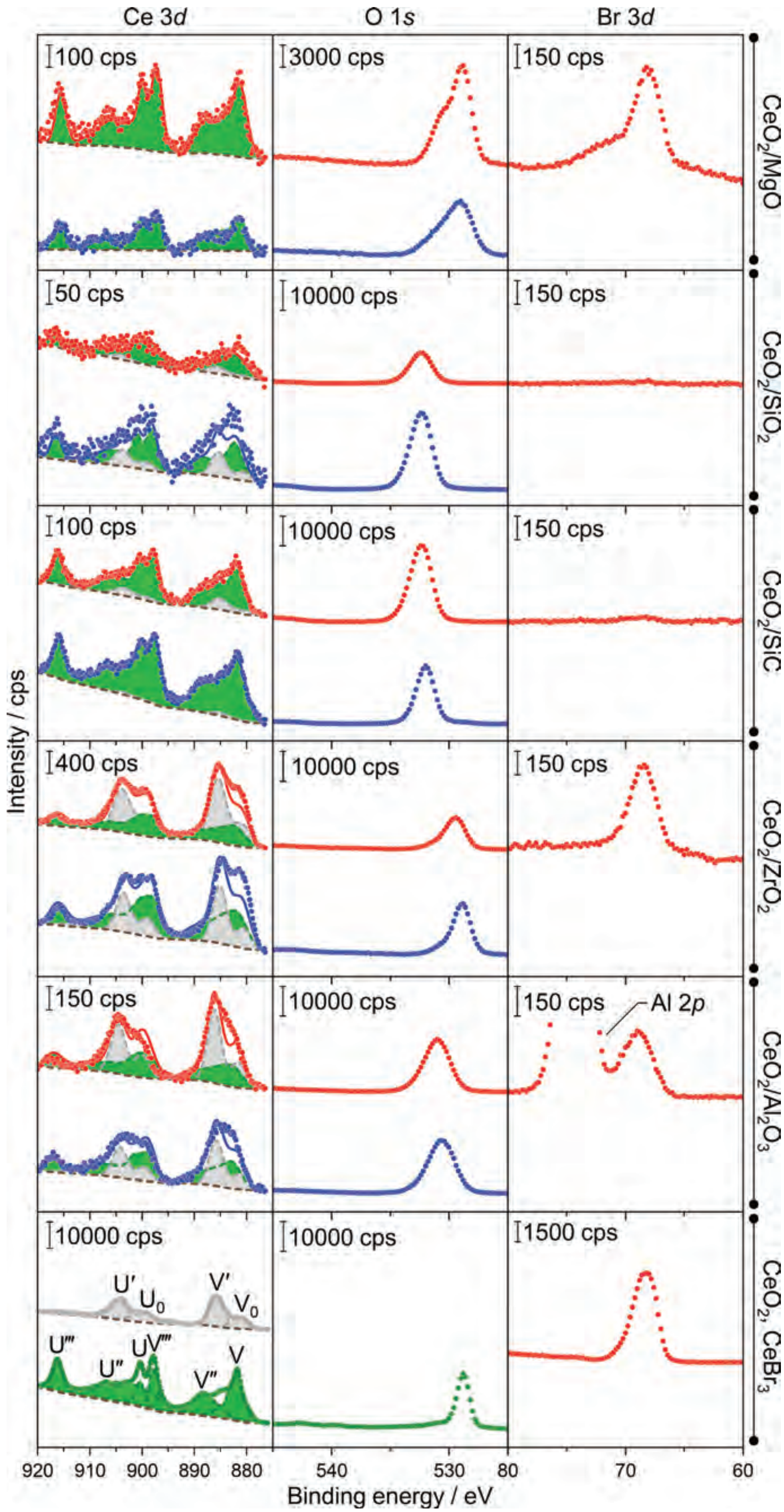

Figure S3. Core level XPS spectra of supported CeO_2 catalysts in fresh form (blue symbols) and after equilibration in methane oxybromination (red symbols). Spectra of the bulk CeO_2 (green symbols) and of $CeBr_3$ (gray symbols) are provided for reference. The positions of the peaks which are characteristic of Ce^{4+} (U, U'', U''', V, V'', V''') and Ce^{3+} (U_0, U', V_0, V') oxidation states are indicated in the bottom left spectra.[1,2] The solid lines behind the respective symbols represent the results obtained by spectral fitting. The dashed brown lines define the used background and the dashed green and gray lines filled with colored areas display the calculated contributions of Ce^{4+} and Ce^{3+} states. Equilibration conditions as reported in the caption of **Figure S2**. Ceria gives a complex set of satellite peak pairs (U'' and V'', U''' and V''') around its 3*d* signals (U and V) associated with shake-up/shake-down.[3] Each pair of satellite peak pairs have the same 18.3 eV separation and 2:3 peak area ratio as the main 3*d* signals. The sharp U''' peak at the high binding energy of *ca*. 916 eV is only associated with Ce^{4+}, and is useful for characterizing the oxidation state of cerium in the supported samples. A more accurate quantitative separation of the Ce 3*d* signal into the relative Ce^{3+} and Ce^{4+} contribution can be obtained by spectral fitting using reference spectra acquired under the same conditions as used to analyze the different supported catalysts.[4] The latter procedure was adopted to estimate the ratio Ce^{4+}:(Ce^{3+}+Ce^{4+}) in the supported CeO_2 catalysts in their fresh form and after equilibration in MOB. Herein, the spectra obtained from fresh CeO_2 and $CeBr_3$ (**Figure S3**, bottom) were used as a reference for Ce^{4+} and Ce^{3+} contributions, respectively. The spectrum of CeO_2 was reproduced by a set of seven Gauss peaks and the spectrum of $CeBr_3$ was reproduced by a set of five Gauss peaks. For each reference all the peaks have been locked in their relative positon, relative area, and FWHM (**Figure S3**, bottom). This allows compensating for different charging during analysis as well as for small peak broadening.

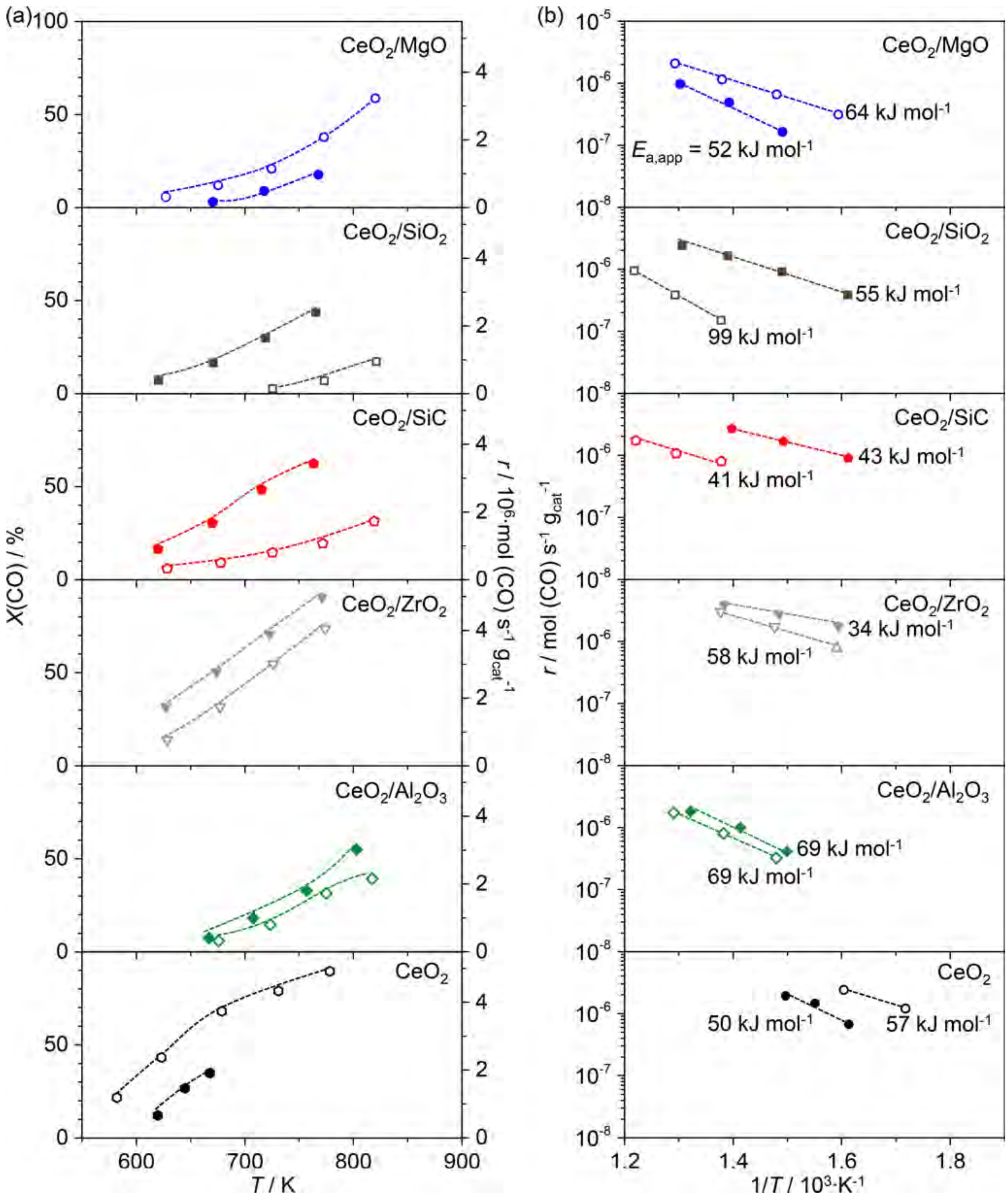

Figure S4. (a) Conversion and rate of CO oxidation over bulk and supported CeO_2 catalysts in fresh form (open symbols) and after equilibration in methane oxybromination (solid symbols), and (b) corresponding Arrhenius plots used to determine the apparent activation energy. Equilibration conditions as reported in the caption of **Figure S2**. Conditions for CO oxidation: $CO{:}O_2{:}Ar{:}He$ = 1.5:3:4.5:91, F_T/W_{cat} = 500 $cm^3\ min^{-1}\ g_{cat}^{-1}$, P = 1 bar. The reaction rates were calculated as the average reaction rate of an integral reactor according to the Eq. 3 of the main manuscript and were primarily used as the parameter to establish the relative order of the catalyst activities in methane oxybromination and different complementary reactions comprising the oxidation of CO, CH_4, HBr, CH_3Br, and CH_2Br_2. The reaction rates reported in the **Figure 5b** of the main manuscript were determined from the lower activity region of the respective light-off curves that corresponds to 5-40% of conversion. This approach, which was also applied in previous studies,[5] provides a comprise between *i*) the errors in the analysis of reactants and products, which tend to propagate under differential reactor operation and relatively low product concentrations, *ii*) linearity of the Arrhenius plots, and *iii*) the axial concentration gradient, which is relatively similar for the different catalysts since the rates were estimated at comparable conversion levels.

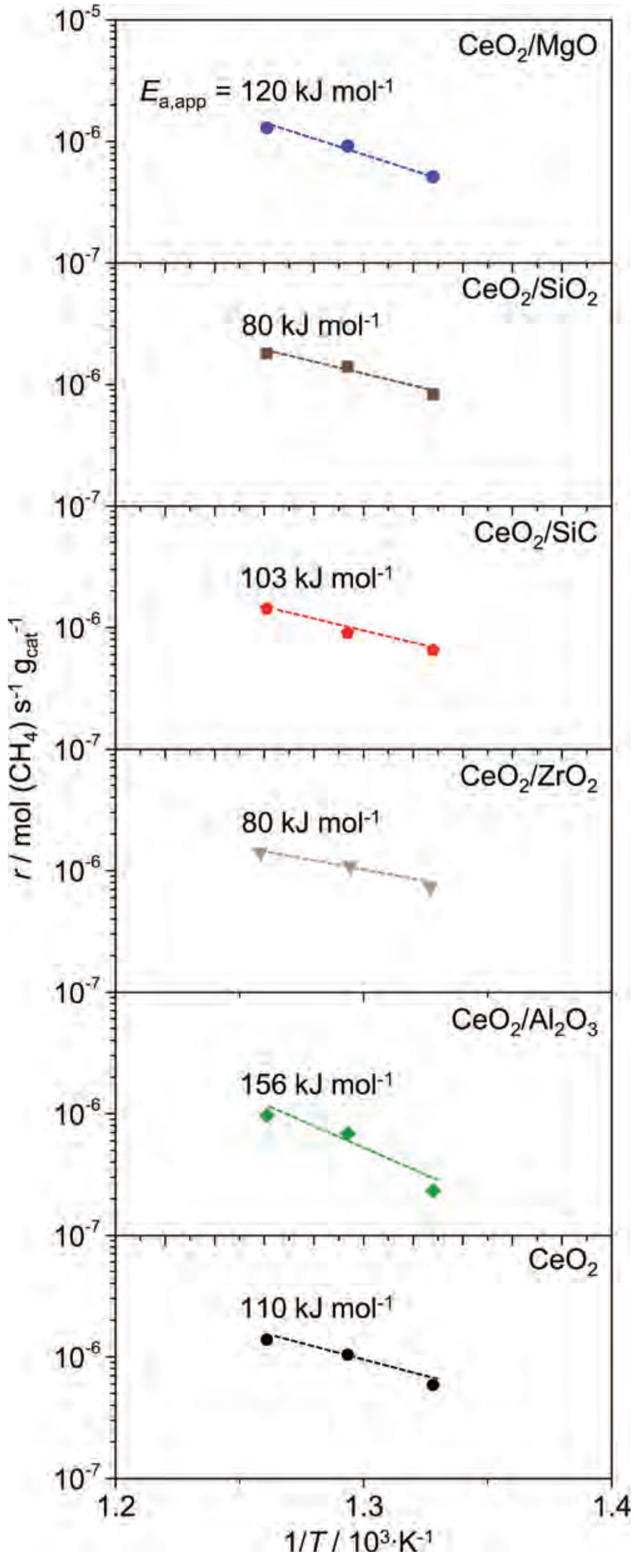

Figure S5. Arrhenius plots used to determine the apparent activation energy of methane oxybromination over bulk and supported CeO_2 catalysts. Conditions: CH_4:HBr:O_2:Ar:He = 6:6:3:4.5:80.5, F_T/W_{cat} = 100 $cm^3\ min^{-1}\ g_{cat}^{-1}$, P = 1 bar. The reaction rates were calculated as reported in the caption of **Figure S4**.

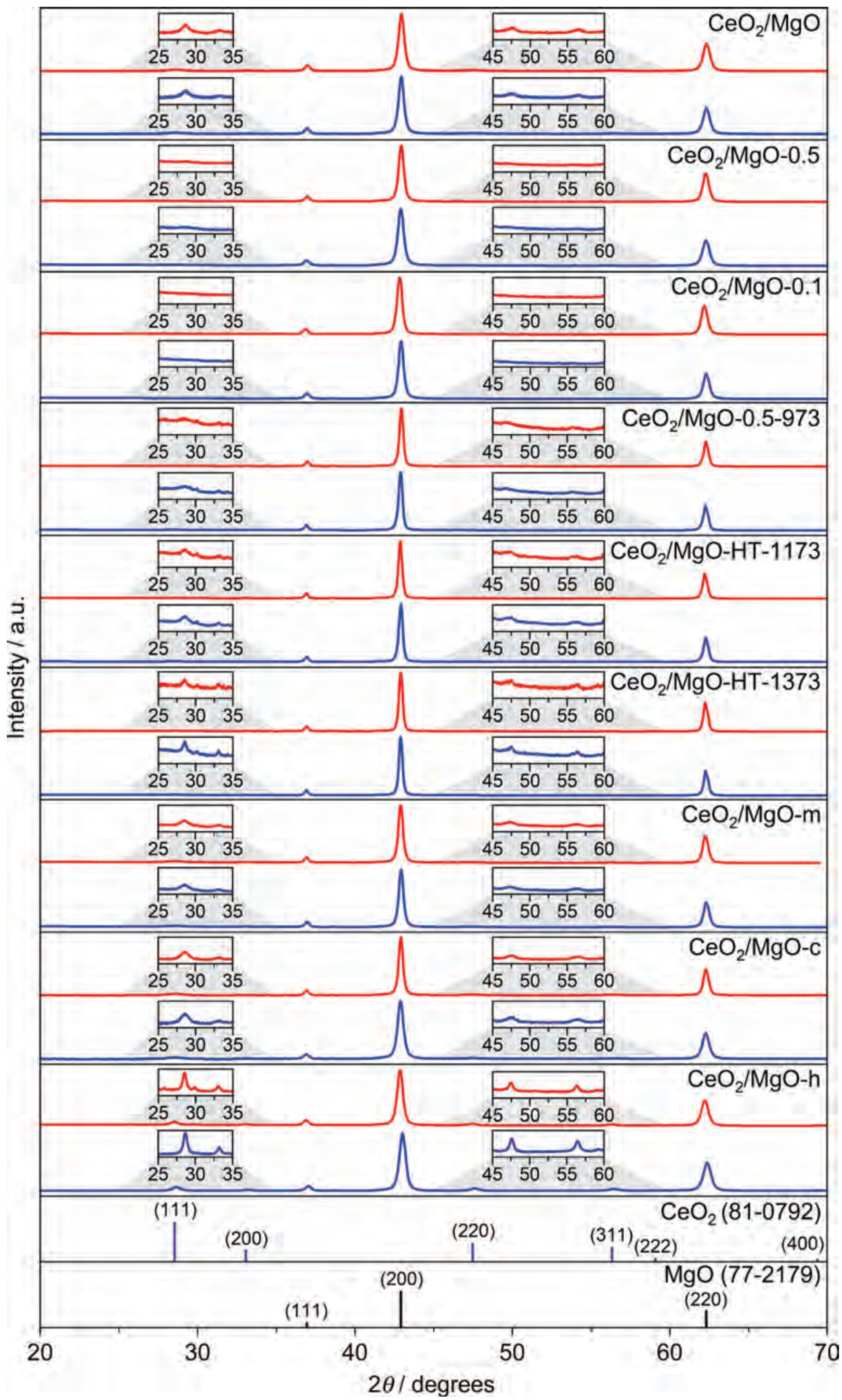

Figure S6. XRD patterns of the MgO-supported CeO_2 catalysts in fresh form (blue) and after equilibration in methane oxybromination (red). Reference patterns shown as vertical lines below the measured diffractograms are identified with their ICDD-PDF numbers. The insets show the magnified parts of the diffractograms in which the main reflections of CeO_2 are expected to appear. Equilibration conditions as reported in the caption of **Figure S2**.

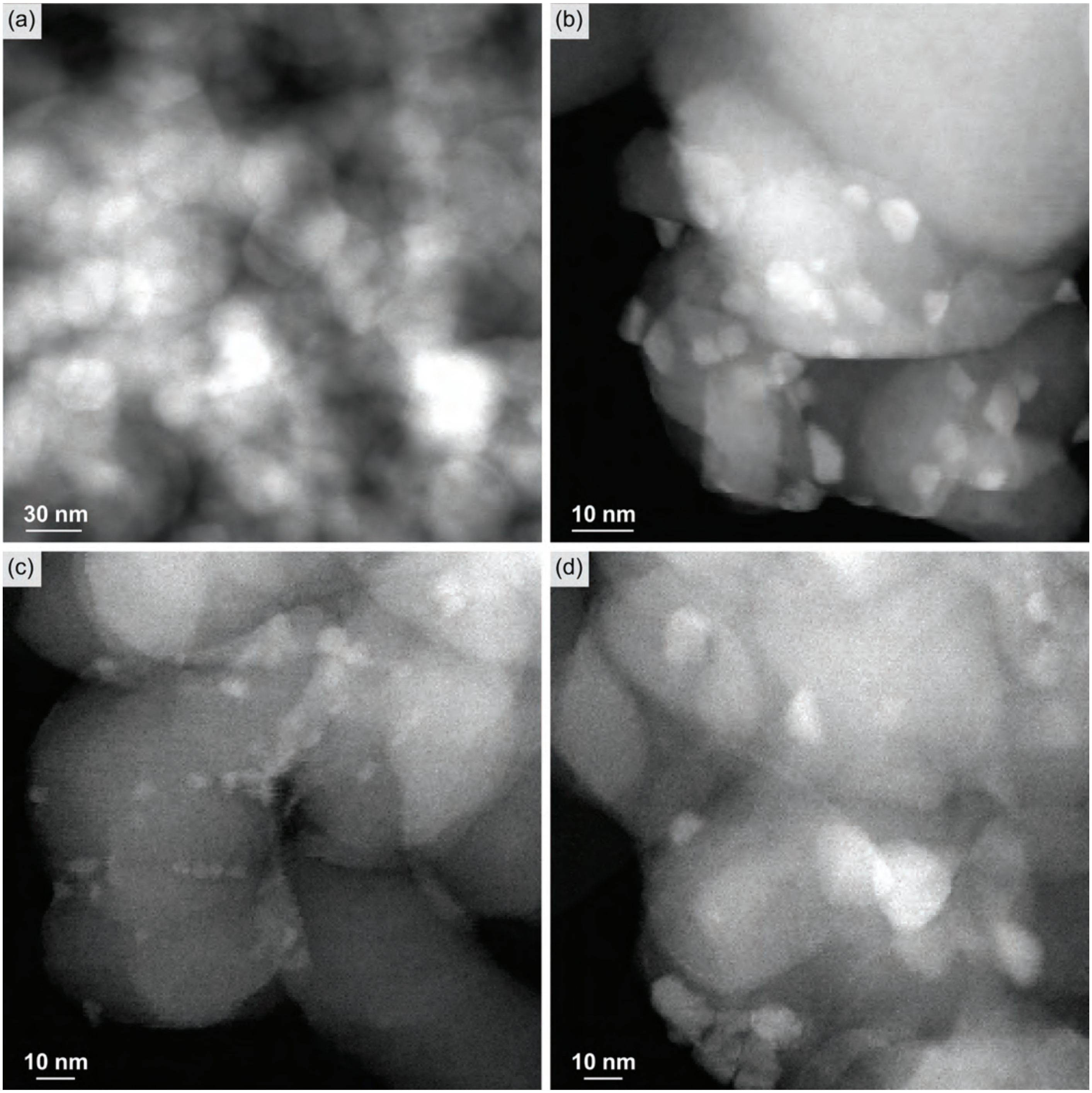

Figure S7. HAADF-STEM micrographs of (a) CeO_2/MgO-0.1, (b) CeO_2/MgO-0.5, (c) CeO_2/MgO-0.5-973, and (d) CeO_2/MgO-0.5-1373 catalysts after equilibration in methane oxybromination. Equilibration conditions as reported in the caption of **Figure S2**.

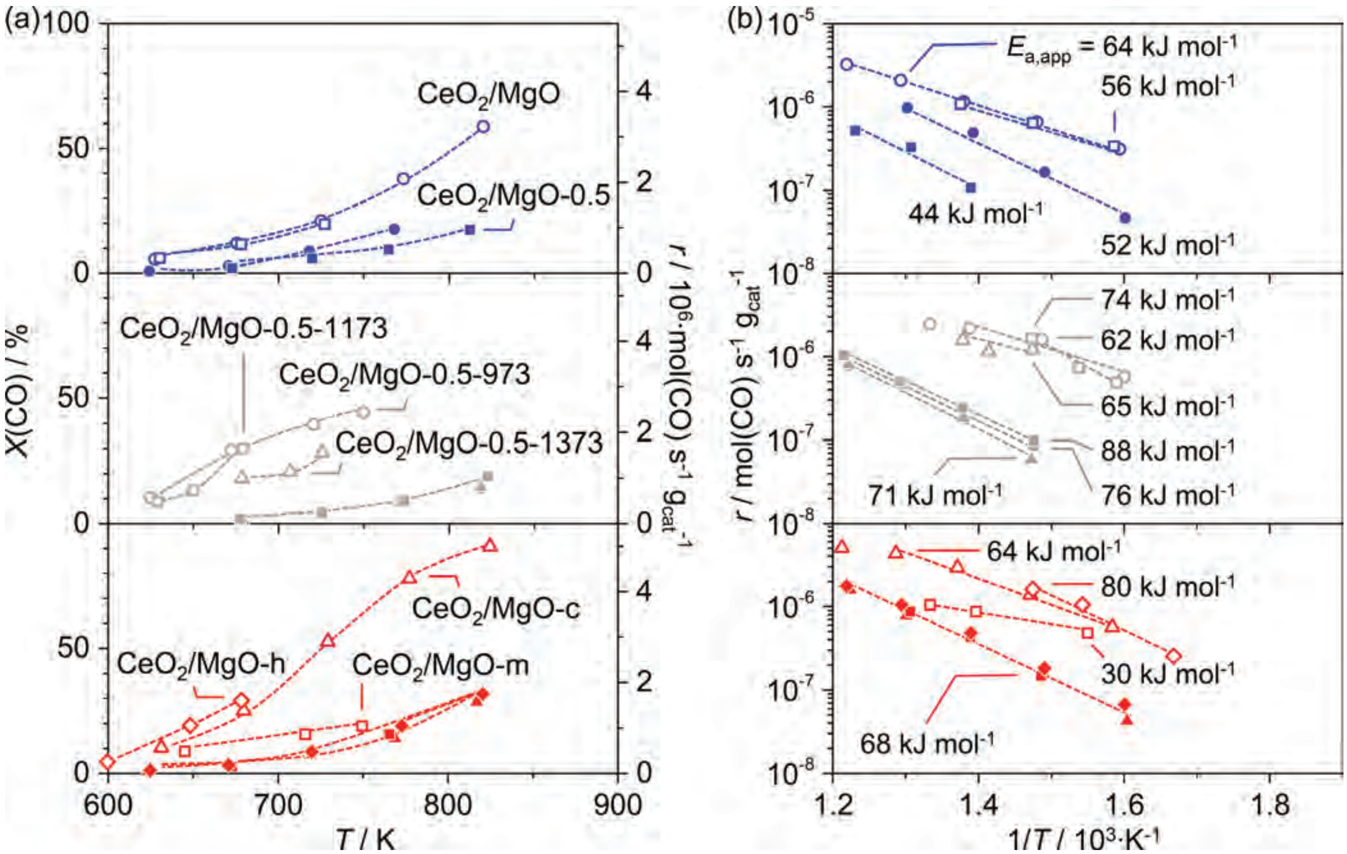

Figure S8. (a) Conversion and rate of CO oxidation over MgO-supported CeO_2 catalysts in the fresh form (open symbols) and after equilibration in methane oxybromination (solid symbols), and (b) corresponding Arrhenius plots used to determine the apparent activation energy. Equilibration conditions as reported in the caption of **Figure S2**. Conditions for CO oxidation: CO:O_2:Ar:He = 1.5:3:4.5:91, F_T/W_{cat} = 500 cm^3 min^{-1} g$_{cat}^{-1}$, P = 1 bar. The reaction rates were calculated as reported in the caption of **Figure S4**.

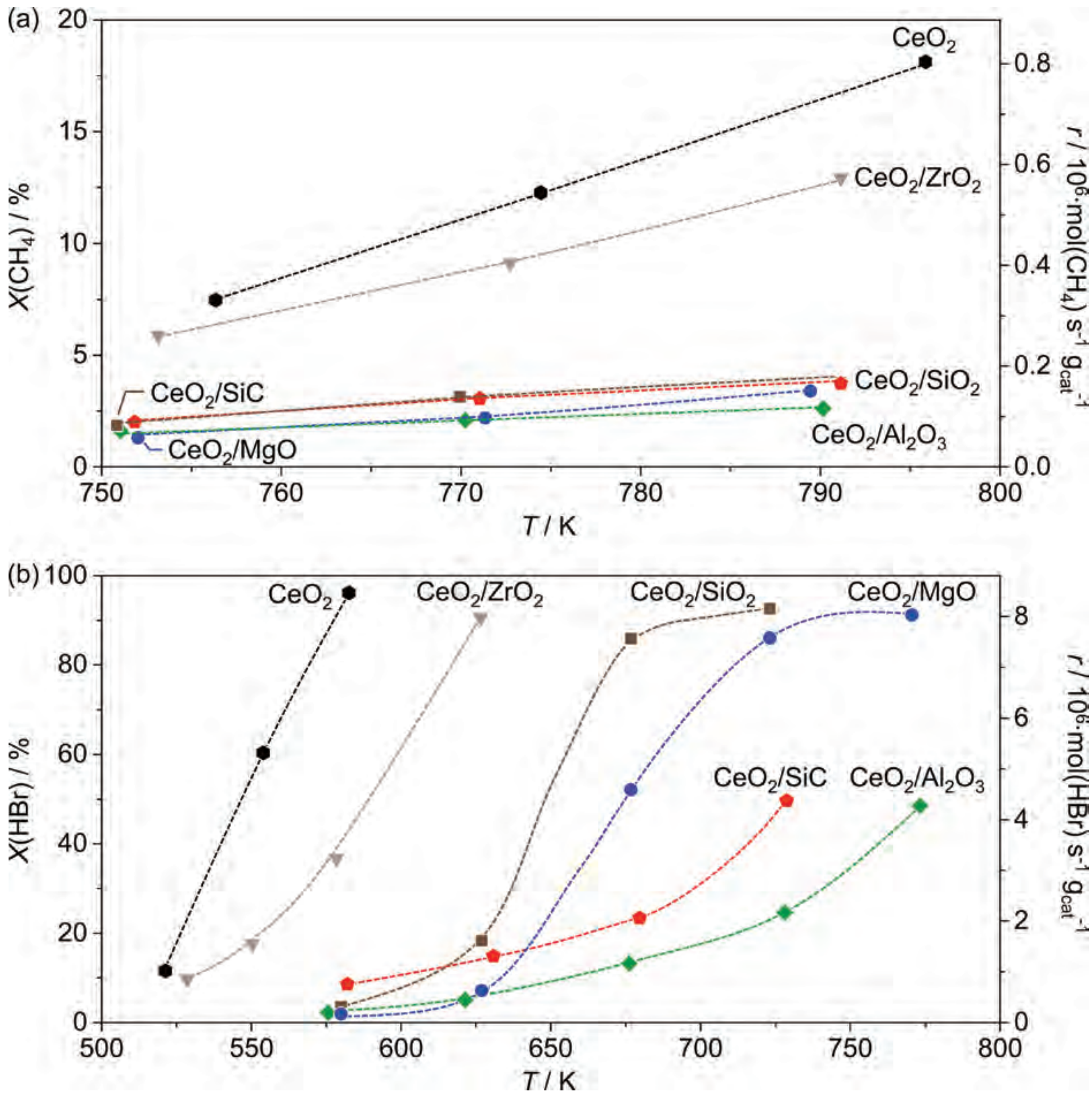

Figure S9. Conversion and rate of (a) methane oxidation (CH_4:O_2:Ar:He = 6:3:4.5:86.5, F_T/W_{cat} = 100 $cm^3\ min^{-1}\ g_{cat}^{-1}$) and (b) HBr oxidation (HBr:O_2:He = 6:3:91, F_T/W_{cat} = 200 $cm^3\ min^{-1}\ g_{cat}^{-1}$) over bulk and supported CeO_2 catalysts after equilibration in methane oxybromination. Equilibration conditions as reported in the caption of **Figure S2**. All the tests were conducted at P = 1 bar. The reaction rates were calculated as reported in the caption of **Figure S4**.

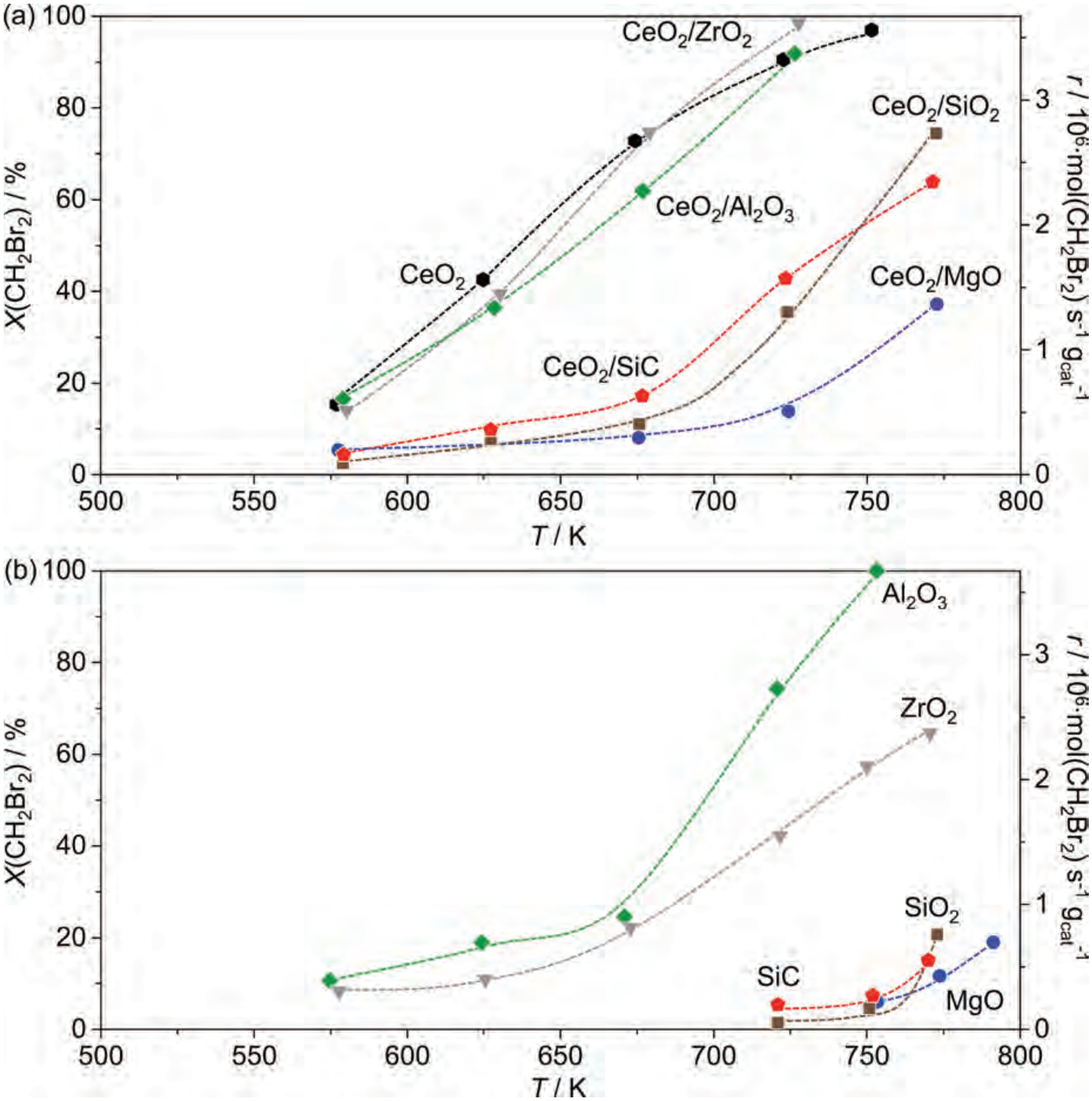

Figure S10. Conversion and reaction rate of CH_2Br_2 oxidation (CH_2Br_2:O_2:Ar:He = 1:2:4.5:92.5, F_T/W_{cat} = 500 $cm^3\ min^{-1}\ g_{cat}^{-1}$) over (a) bulk and supported CeO_2 catalysts, and (b) the carriers after equilibration in methane oxybromination. Equilibration conditions as reported in the caption of **Figure S2**. All the tests were conducted at P = 1 bar. The reaction rates were calculated as reported in the caption of **Figure S4**.

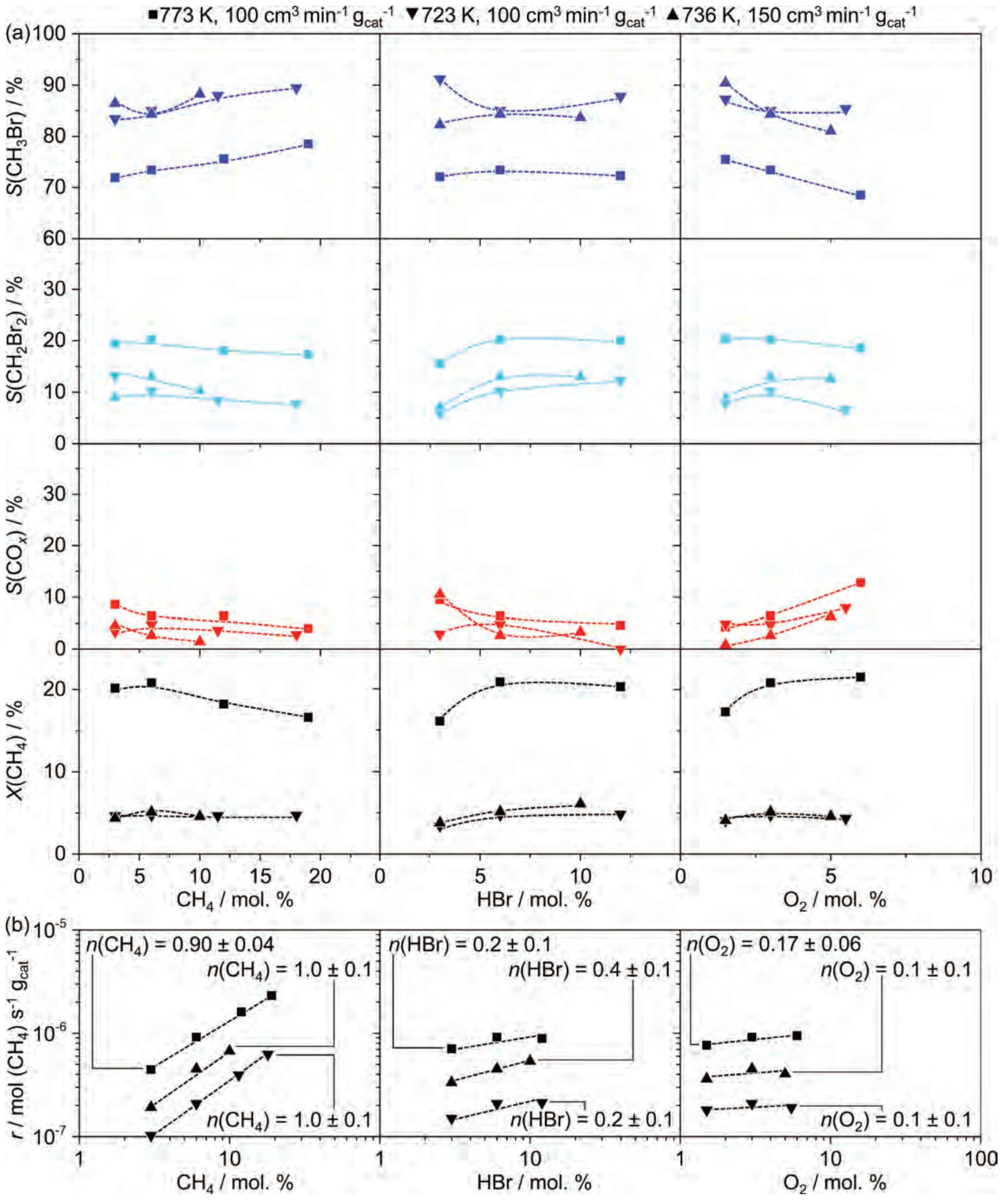

Figure S11. (a) Conversion of methane and product selectivity and (b) rate of methane oxybromination *versus* the feed concentrations of methane (CH_4:HBr:O_2:Ar:He = 3-20:6:3:4.5:80.5-66.5), hydrogen bromide (CH_4:HBr:O_2:Ar:He = 6:3-12:3:4.5:83.5-74.5), and oxygen (CH_4:HBr:O_2:Ar:He = 6:6:1.5-6:4.5:82-77.5) over

CeO_2/MgO at different space velocities (F_T/W_{cat} = 100 or 150 cm^3 min^{-1} g_{cat}^{-1}) and temperatures (T = 723-773 K). All the tests were performed at P = 1 bar. The apparent reaction orders with respect to methane, $n(CH_4)$, hydrogen bromide, n(HBr), and oxygen, $n(O_2)$, are reported in the corresponding plots in (b). The reaction rates were calculated as reported in the caption **Figure S4**. In the experiments performed at T = 723 K, F_T/W_{cat} = 100 cm^3 min^{-1} g_{cat}^{-1}, and 736 K, F_T/W_{cat} = 150 cm^3 min^{-1} g_{cat}^{-1} the conversion of methane was in range 3-6%, at which the rate computed by Equation 3 of the main manuscript shows a relatively small deviation from the initial rate.

REFERENCES

(1) Engelhard, M.; Azad, S.; Thevuthasan, S. *Surf. Sci. Spectra* **2005**, *11*, 73-81.

(2) Mullins, D. R. *Surf. Sci. Rep.* **2015**, *70*, 42-85.

(3) Gore, C. M.; White, J. O.; Wachsman, E. D.; Thangadurai, V. *J. Mater. Chem. A* **2014**, *2*, 2363-2373.

(4) Holgado, J. P.; Alvarez, R.; Munuera, G. *Appl. Surf. Sci.* **2000**, *161*, 301-315.

(5) Farra, R.; García-Melchor, M.; Eichelbaum, M.; Hashagen, M.; Frandsen, W.; Allan, J.; Girgsdies, F.; Szentmiklósi, L.; López, N.; Teschner, D. *ACS Catal.* **2013**, *3*, 2256-2268.